

Planetary Nebulae towards the Galactic bulge.

I. [OIII] fluxes

Anna V. Kovacevic^{1*}, Quentin A. Parker^{1,2}, George H. Jacoby³, Rob Sharp⁴, Brent Miszalski⁵ and David J. Frew¹

¹*Department of Physics, Macquarie University, North Ryde, NSW 2109, Australia*

²*Anglo-Australian Observatory, PO Box 296, Epping, NSW 1710, Australia*

³*NOAO, 950 North Cherry Ave. Tucson, AZ 85719, USA*

⁴*Research School of Astronomy & Astrophysics, Mount Stromlo Observatory, Cotter Road, Weston ACT 2611, Australia*

⁵*Centre for Astrophysics Research, STR1, University of Hertfordshire, College Lane Campus, Hatfield AL10 9AB, UK*

Accepted 2010 MONTH XX. Received 2010 MONTH XX; in original form 2010 MONTH XX

ABSTRACT

We present [OIII] λ 5007 fluxes and angular diameters for 435 Planetary Nebulae (PN) in the central $10^\circ \times 10^\circ$ region towards the Galactic bulge. Our sample is taken from the new discoveries of the MASH PN surveys as well as previously known PN. This sample accounts for 80 per cent of known PN in this region. Fluxes and diameters are measured from narrow-band imaging with the MOSAIC-II camera on the 4-m Blanco telescope at the Cerro-Tololo Inter-American Observatory. This is the largest (~ 60 square degrees), uniform [OIII] λ 5007 survey of the inner Galactic bulge ever undertaken. 104 of the objects have measured [OIII] λ 5007, [OIII] λ 4959, H α or H β fluxes from the literature, which we use to undertake a detailed comparison to demonstrate the integrity of our new fluxes. Our independent measurements are in excellent agreement with the very best literature sources over two orders of magnitude, while maintaining good consistency over five orders of magnitude. The excellent resolution and sensitivity of our data allows not only for a robust set of homogenous PN fluxes, but provides greater detail into their intricate, otherwise undetermined [OIII] λ 5007 morphologies. These new, extensive measurements significantly increase the sample of reliable [OIII] λ 5007 fluxes for Galactic bulge PN making it a valuable resource and a prelude to the construction of our new Galactic bulge Planetary Nebula luminosity function (Paper II).

Key words: planetary nebulae, planetary nebula luminosity function, Galactic bulge

1 INTRODUCTION

Since the realisation that the Planetary Nebula luminosity Function (PNLF; Jacoby, Ciardullo & Ford 1988) can be used as a standard candle, it has been firmly established as a reliable extra-galactic distance indicator for galaxies out to the Virgo (18.0 ± 1.2 Mpc; Fouqué et al. 2001) and Fornax (18.6 ± 0.6 Mpc; Madore et al. 1999) clusters and beyond (Jacoby, Ciardullo, & Ford 1990; Feldmeier, Jacoby, & Phillips 2007; Gerhard et al. 2007; Ciardullo 2009). Agreement with traditional population-I distance indicators such as Cepheids and SN Ia (Ciardullo 2003) provides us with a rare link with which we can compare these independent methods between very different stellar populations of different ages and metallicities. However,

despite the robustness of the PNLF as a distance indicator, the underlying detailed physics responsible is not well understood. The strength of the PNLF distance technique resides in the fit of the PNLF function having a definitive absolute magnitude bright-end cut-off at $M_{[\text{OIII}]}$ = $-4.47^{+0.02}_{-0.03}$ (Ciardullo et al. 2002), regardless of galaxy type and age, though there does appear to be a small dependence on metallicity (Dopita, Jacoby, & Vassiliadis 1992). Ciardullo et al. (2005) outlined this fundamental inconsistency. The PN at the bright-end of the PNLF have central star luminosities of $\sim 6000 L_\odot$, which requires the central stars to be $> 0.6 M_\odot$ (Méndez et al. 2008; Marigo et al. 2004) and corresponds to a mass on the main-sequence of $> 2 M_\odot$ (Weidemann 2000). Stars with such main-sequence masses, and consequent short lifetimes ($\sim 1\text{-}2$ Gyr), are not expected to be present in elliptical galaxies whose populations are typically ~ 10 Gyr old and where there is no evidence for recent star formation. However, the bright PN

* Correspondence to E-mail: akovac@ics.mq.edu.au

that have evolved from such stars are nonetheless detected in these populations.

This conundrum has been a major obstacle in our interpretation and understanding of the apparently fixed nature of the bright-end of the PNLF across galaxy types for nearly 20 yrs. To address the problem we urgently need to deconstruct the PNLF in fine detail.

To evaluate the varied characteristics of individual PN constituting the PNLF, we require a self-contained system at a known distance whose PN population is sufficiently nearby to permit investigation into individual PN morphologies, their abundances, expansion velocities, central star temperatures and consequently their masses. Such detailed analyses can be achieved in relatively nearby galaxies such as the LMC (Reid & Parker 2010) and SMC (Jacoby & De Marco 2002), but being metal-poor and comprised of intermediate-age populations they cannot represent valid proxies for an old elliptical galaxy and cannot be used to address the problem outlined above.

Fortunately, the bulge of our Galaxy, being relatively nearby (~ 8 Kpc), has the potential to represent such a system. There is mounting evidence that our Galactic bulge formed within a very short time-scale (Rich & Origlia 2005; Zoccali et al. 2006; Fulbright, McWilliam, & Rich 2007) about ~ 10 Gyr ago (Ortolani et al. 1995; Feltzing & Gilmore 2000; Zoccali et al. 2003). A rapid star formation history in the early universe indicates that early-type spiral bulges undergo a comparable formation mechanism to elliptical galaxies (Peletier et al. 1999; Falc3n-Barroso, Peletier, & Balcells 2002). We can therefore exploit its proximity and population age as a proxy for an elliptical galaxy amenable to detailed study.

This work has the potential to determine whether the PNLF bright-end is comprised of PN resulting from old, population-II stars which have found some peculiar path to enhanced luminosity, e.g. through binarity (Ciardullo et al. 2005; Miszalski et al. 2009a), or if it is in fact dominated by younger, higher mass, bipolar nebulae mainly of Type-I as defined by Kingsburgh & Barlow (1994) and Torres-Peimbert & Peimbert (1997). These are thought to derive from more massive progenitors which suffer third dredge-up and undergo hot-bottom burning, subsequently becoming nitrogen and helium enriched. Such detailed analysis of an old stellar population is currently, and for the foreseeable future, impossible to do anywhere else. The next nearest old population is the bulge of M31 and in order to obtain spectra of comparable quality/depth to what exists for Galactic bulge PN requires instrumentation beyond what is currently available. Hence, this work will provide a significantly improved understanding of the PN population in all elliptical galaxies as well as in spiral bulges.

Our ability to study such samples has been recently enhanced thanks to the highly sensitive AAO/UKST SuperCosmos H α Survey of the southern Galactic plane (SHS; Parker et al. (2005)) which enabled doubling the number of known bulge PN in this region as reported in the Macquarie/AAO/Strasbourg H α PN catalogues of Parker et al. (2006) and Miszalski et al. (2008), dubbed MASH and MASH-II. This combined sample is more representative of

the bulge PN population spanning a wider evolutionary range and allows us here to construct a new [OIII] $\lambda 5007$ Galactic bulge PNLF of unprecedented coverage. This will enable detailed study of the various sub-sets of PN (whether Type-I chemically or of certain morphologies) within the PNLF, whether they are confined to certain regions within the PNLF and, importantly, whether one population sub-set is solely responsible for constituting the bright-end. These analyses will be presented in Kovacevic et al. (2010b), hereafter Paper II, while this paper describes the process for defining robust [OIII] $\lambda 5007$ flux measurements.

2 OBSERVATIONS

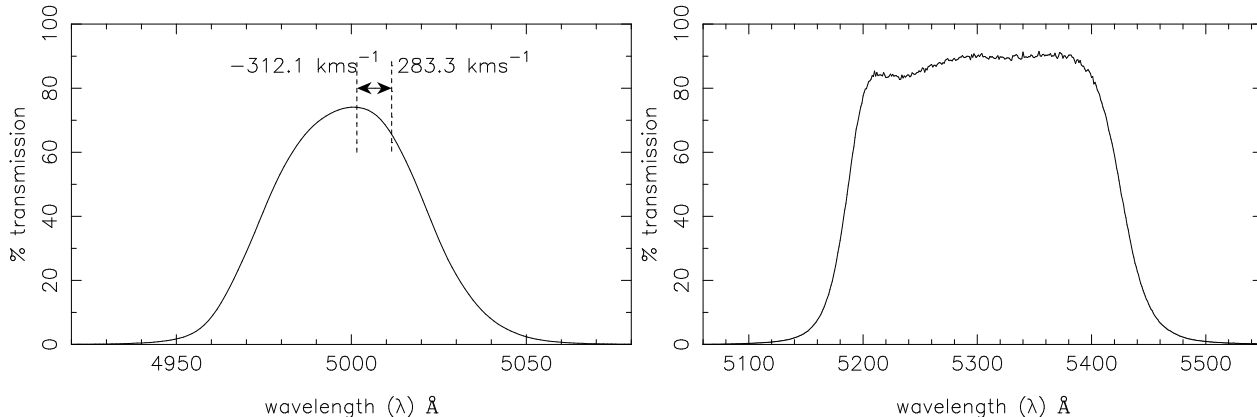
We observed previously known and MASH PN in a $10^\circ \times 10^\circ$ region toward the Galactic bulge using the Cerro-Tololo Inter-American Observatory (CTIO) 4-m Blanco telescope in Chile with the MOSAIC-II CCD Imager (Muller et al. 1998). This instrument provides a field of view (FoV) of $\sim 36' \times 36'$, using a mosaic of eight SITe 2048×4096 pixel CCDs, at a scale of ~ 0.27 arcsec pixel $^{-1}$. A total of ~ 95 hours of photometric imaging was conducted, spread over two observing runs: 6 nights throughout 9th – 14th June 2008 and 5 nights from 27th June – 2nd July 2009. The weather was consistently photometric throughout the first run with a modest seeing range from 0.7 – 1.0 arcsec, with only 1.5 hours lost to technical and software faults. The weather was significantly more variable throughout the 2009 run, resulting in a loss of 2.5 nights. In photometric conditions, the seeing varied from 1.0 – 2.0 arcsec, with extremes of 2.5 arcsec. Exposure times comprised of 3×400 second in the [OIII] $\lambda 5007$ band, an additional 60 second exposure for those fields containing bright PN to avoid saturation, and 3×90 second exposures in the broader, [OIII] $\lambda 5007$ -off band filter. In the 2009 run we modified the number of off-band exposures to 2 in order to cover a wider area while still reaching an adequate depth. Filter details are given in Table 1, while the transmission curves of the [OIII] $\lambda 5007$ on- and off-band filters are shown in Fig. 1. The [OIII] $\lambda 5007$ transmission curve was measured by NOAO with a simulated $f/2.9$ beam for the CTIO 4-m 1 , whilst the off-band transmission curve was measured with a simulated $f/3.1$ beam for the KPNO 4-m, so should be $\sim 3\text{\AA}$ bluer when used on the CTIO 4-m. In addition, spectrophotometric standard stars were observed at the beginning, middle and end of each night to allow for flux calibration of the fields.

As part of general follow-up, we also have obtained 100 per cent spectroscopy for all MASH PN in the bulge sample (Parker et al. 2006; Miszalski et al. 2008), including at high resolution for radial velocity determination. Although the spectra were primarily taken for identification and radial velocity purposes, they can give initial estimates of the Balmer decrement in many cases. These can be used to provide preliminary dereddened fluxes (see section 4.4).

¹ Filter curves can be found at <http://www.ctio.noao.edu/mosaic/manual/index.html>

Table 1. Filters used in the CTIO observing runs.

Filter	NOAO code	$\lambda_{central}$ (Å)	FWHM (Å)
[OIII] λ 5007	c6014	5000	50
[OIII] λ 5007+30nm	k1015	5320	240
H α + [NII] λ 6548, 6583	c6009	6563	80
H α +8nm	c6011	6650	80

**Figure 1.** The f/2.9 transmission curve of the [OIII] λ 5007 (left) and off-band [OIII] λ 5007 filter (right) used. The wavelength shift of the [OIII] λ 5007 line experienced by the PN with largest positive and negative velocities are shown here. The filter transmission experienced by these two PN is 74.07 per cent and 64.71 per cent, respectively.

2.1 Strategy

The large field-of-view ($36' \times 36'$) of the MOSAIC-II camera allowed for the observation of ~ 4 PN per field. Placement of fields were chosen manually using the Aladin software (Bonnarel et al. 2000), with a MOSAIC-II template especially provided. For regions where the PN number density was significantly higher, the field placement was arranged in a tiled manner, allowing an overlap of $\sim 2'$ between fields. This applied to the $358^\circ \leq l \leq 2^\circ$ and $-1^\circ \leq |b| \leq -3^\circ$ region. For the remaining area, field placement was chosen such that the number of fields was minimised whilst ensuring observation of a maximum number of PN. Fig. 2 illustrates the coverage of survey fields.

Approximately 150 pointings were needed to obtain [OIII] λ 5007 images for all PN in this region. We were able to observe 124 fields, covering 80 per cent of all MASH and previously known PN in the $10^\circ \times 10^\circ$ region towards the Galactic bulge. Table A1 lists the identification assigned (column 1) of the fields observed, and their central co-ordinates in RA (column 2) and declination (column 3) with the exposure times of images (column 4). To avoid incompleteness in specific regions of the bulge due to potential adverse weather conditions during either run, we decided to focus each run on observations of either the north or south of the bulge. As the southern half of the bulge is the most densely populated with PN (suffering lower extinction), we largely dedicated our 2008 run to observing PN in this half, and observed northern PN on our 2009 run. As the northern bulge rises ~ 30 mins before the southern half, we were also able to observe one northern bulge field in the 2008 run, and an extra

southern bulge field in the 2009 run. The majority of fields were observed at an airmass of ≤ 2 .

2.2 Resolution and uniformity

The uniformity of this [OIII] λ 5007 survey not only provides accurate fluxes for the largest sample of bulge PN to date, but the high resolution of the MOSAIC-II camera allows for precise angular diameter measurements (see section 5) and a greater insight into the details of the morphologies of these predominantly compact PN than previously available. Better, well-defined classifications of PN morphologies can provide clues as to their modes of evolution (Miszalski et al. 2009a,b; Kwok 2010), and can therefore help isolate sub-sets of the PN population when analysing their placement on the PNLF. This issue will be addressed further in Paper II in this series.

3 REDUCTIONS

The data were reduced using the Cambridge Astronomical Software Unit (CASU) pipeline/toolkit (Irwin & Lewis 2001). Although this toolkit was originally written for the Wide-Field Imager on the Isaac-Newton Telescope (INT), additional software was available to extract systematic errors specific to MOSAIC-II data.

Photometry was performed on the cross-talk corrected (e.g. see Freyhammer et al. 2001), bias-subtracted, flat-fielded, astrometrically calibrated, continuum-subtracted images. Multiple images of the same field were taken to both avoid CCD saturation issues and then stacked to

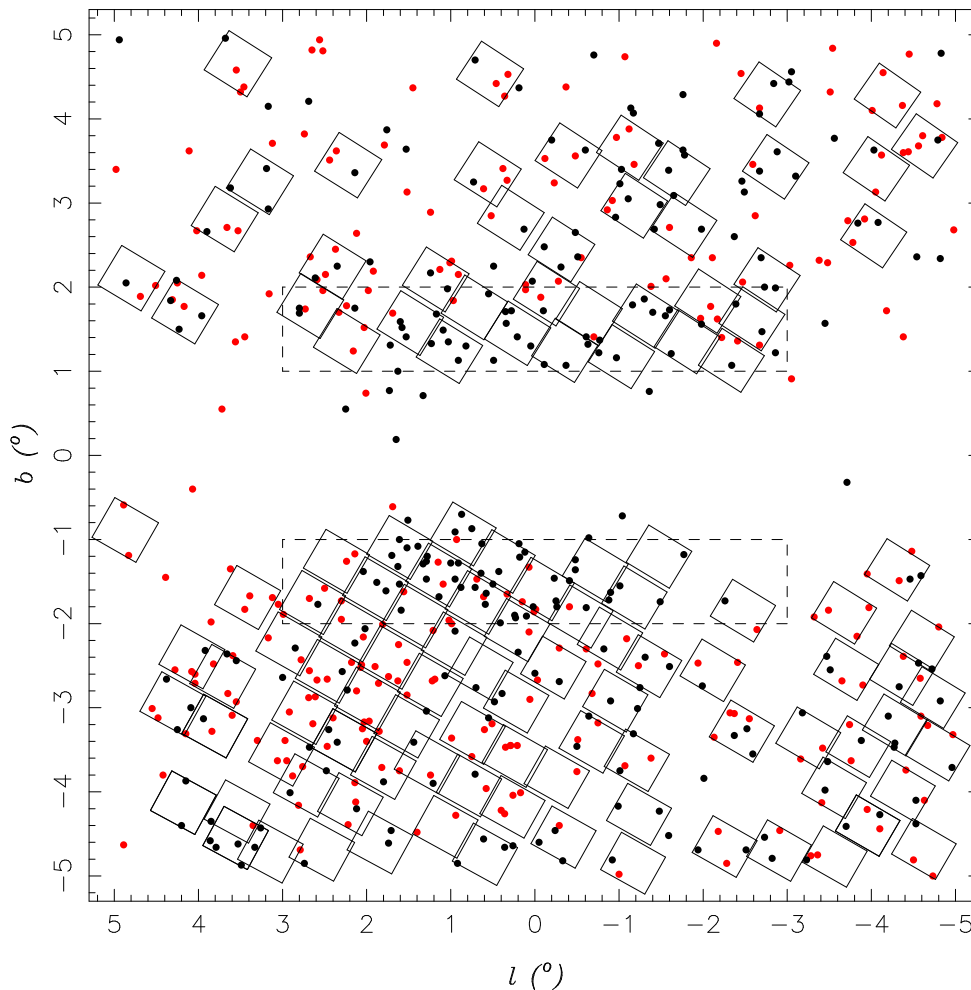


Figure 2. Placement of the fields in the direction of the Galactic bulge. The dots illustrate the distribution of PN, the red circles being MASH-I and MASH-II PN while the black circles represent previously known PN. The squares are the observed MOSAIC-II fields.

eliminate cosmic-rays present in the images. The USNO-A2.0 catalogue was used to derive the astrometric fit. Removal of the stellar and background continuum for each field was achieved by comparing intergrated counts of ~ 50 stars in the off-band image to the $[\text{OIII}] \lambda 5007$ image. This determined a flux scaling factor which, once applied to the off-band image, ensured approximately equivalent depths for continuum point sources between bands. The off-band image was then brought into alignment to the on-band image by applying the XREGISTER routine in IRAF. This removed any non-integer pixel shifts in the x- and y-direction, and accounted for any rotational and stretching effects. The off-band image was then subtracted from the on-band image. This procedure was successful in the effective removal of stars for the majority of bulge fields, but not so for fields that exhibited very high stellar number densities.

Fluxes were then measured using the aperture photometry utility within GAIA², with the average sky determined via a clipped mean, in order to exclude deviant pixels from

the calculation. Aperture sizes were chosen to be as large as possible without inclusion of any badly-subtracted stars. The flux contributions of such artefacts were individually taken into account when they directly overlaid the nebula. Such instances were of common occurrence in extended PN ($\gtrsim 20$ arcsec). Fluxes were only measured for the bright PN where the maximum pixel value was $\lesssim 30000$ counts, as the MOSAIC-II CCDs are documented³ to show non-linear characteristics beyond ~ 35000 counts per pixel.

3.1 Flux calibration

The $[\text{OIII}] \lambda 5007$ fluxes were calibrated in units of $\text{erg s}^{-1} \text{cm}^{-2}$ relative to the following spectrophotometric standards: EG 274, LTT 9491, LDS 749B, LTT 4816, GD 108 and LTT 7987, whose spectra are highly sampled and are well-documented in the literature (Bohlin 1996; Hamuy et al. 1992). The flux calibration procedure followed that of Jacoby, Africano, & Quigley (1987). The integral under the filter curve was multiplied by the flux at

² <http://www.starlink.ac.uk/gaia>

³ <http://www.noao.edu/ctio/mosaic/>

5006.8Å (the rest wavelength of the [OIII] λ5007 line) and divided by the count rate of the standard star to achieve a system sensitivity in $\text{ergs s}^{-1} \text{cm}^{-2} \text{count}^{-1}$. The global counts from each PN were then converted into a count rate by dividing by the length of exposure time and corrected for atmospheric extinction which was taken to be 0.17 mag/airmass (Hamuy et al. 1992).

The radial velocities of the PN were utilised to determine the shift of the [OIII] λ5007 line, and consequently to determine the transmission of the filter at that wavelength. This is especially important for bulge PN as they can have relatively high velocities ($\sim \pm 300 \text{ km/s}$). Additionally, the shape of the filter displayed a gaussian-like profile, so the transmission through the filter for the PN with the most negative velocity (74.07 per cent) was significantly different than that from the PN with the most positive velocity (64.71 per cent). These fluxes would have been subjected to an additional error of $\pm_{0.02}^{0.05}$ in the $-\log F$ had this not been taken into account. The bulk of non-MASH PN velocities were taken from Durand, Acker, & Zijlstra (1998) and the remainder were taken from Miszalski et al. (2011) (hereafter D98 and M11, respectively). The velocity measurements from these two sources combined account for all but 34 of the objects measured. To ensure consistency, velocity measurements from other sources such as low dispersion object prism spectra were not considered. Fluxes were then calculated by converting a count rates to a flux via multiplication by the system sensitivity.

4 [OIII] λ5007 FLUXES

We present both our observed [OIII] λ5007 global fluxes and preliminary dereddened fluxes, and angular diameters for 435 PN in the $10^\circ \times 10^\circ$ region toward the Galactic bulge in Table A2, supplemented by a further 6 outside of this region, bringing the total observed to 441.

In this central bulge $10^\circ \times 10^\circ$ sector, the literature contains directly measured [OIII] λ5007 fluxes for 48 PN, therefore this paper is contributing new fluxes for 387 PN in this region. Their IAU PN G and common names are listed in the first two columns of Table A2, the observed [OIII] λ5007 flux measured directly from the CCD image is presented in column (3) (in $\text{erg cm}^{-2}\text{s}^{-1}$) with their estimated errors in column (4), while their preliminary dereddened [OIII] λ5007 flux is listed in column (5). Their major and minor axes (in arcsec) are listed in columns (6) and (7). We have tabulated five other known PN that were observed in the peripheral region and the recently discovered open cluster PN (Parker et al. 2010) in Table A3. PN that display no observable flux are tagged as non-detections where they are either too cool to produce [OIII] λ5007 emission or too heavily reddened to meet our detection/sensitivity limit. Fluxes were dereddened for those PN with suitably calibrated DBS or AAOmega spectroscopy. This was available for ~ 60 per cent of those PN with observed fluxes.

4.1 Error analysis

Total errors in our observed flux measurements were derived for each PN. These took into account the errors due to the strength of the signal, the velocities of the PN,

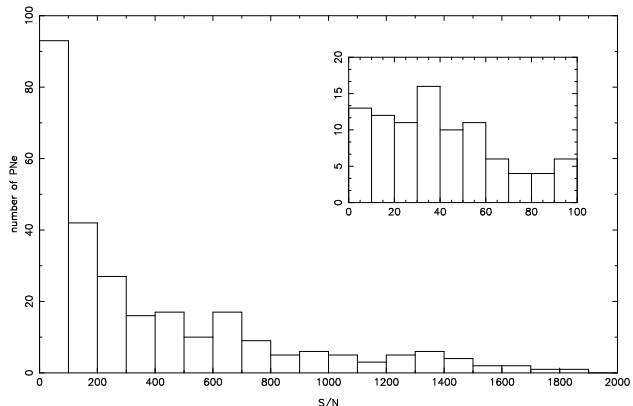


Figure 3. Distribution of S/N measurements. The inset graph magnifies the distribution $0 < S/N \leq 100$. Only 13 PN have S/N less than 10.

the transmission profile of the filter curve, and those due to variation in the sensitivity factor calculated from the spectrophotometric standard stars.

The error due to the signal strength was determined using the full CCD photometric S/N calculation as given in equation (1) (Merline & Howell 1995).

$$\frac{S}{N} = \frac{N_* \times G}{\sqrt{N_* \times G + n_{pix}(1 + n_{pix}/n_B)(N_S \times G + N_D + N_R^2 + G^2 \sigma_f^2)}} \quad (1)$$

Where N_* is the sky-subtracted, summed counts within the aperture, n_{pix} is the number of pixels in the area of the aperture, N_S is the average counts of the background sky per pixel, n_B is the number of pixels that have been used to determine N_S , N_D is the number of dark current electrons per pixel, N_R is the number of electrons per pixel due to read-out noise, G (e^-/ADU) is the gain of the CCD, and σ_f^2 is the estimate of the 1 sigma error introduced within the A/D converter. The denominator comprises all of the relevant factors that contribute to the noise for an ideal system.

The conversion from ADUs to electron counts was achieved via multiplication of the pixel counts by the gain of the CCD, which is $2 e^-/\text{ADU}$ for the SITe CCDs on the MOSAIC-II camera. They have a read-out noise of $6-8e^-$ and a dark-current of $\lesssim 2 e^- \text{pixel}^{-1} \text{hour}^{-1}$. As the areas of the apertures may be considerable in the case of extended PN, it is important that we retain a constant ratio between the area of the nebula aperture and the total area of the sky aperture used, $(1 + \frac{n_{pix}}{n_B})$.

Fig. 3 displays the distribution of S/N measurements for all PN we observed. This only shows those measurements whose $S/N \leq 2000$. There were 8 measurements of bright PN which exceeded this. The S/N distribution within the $0 < S/N \leq 100$ range is relatively flat, with only 13 PN, or 0.3 per cent of the population, having low $S/N < 10$.

The magnitude of flux error due to the uncertainty in the velocities were determined from the errors published in the D98 and M10 sources. At the time of communication, small errors (typically $\sim 1-5 \text{ kms}^{-1}$) were only available for

half of the M10 sample (called M1), so we calculated velocity errors for the remaining PN (sample M2) via calculation of the standard deviation σ of the difference between the M1 and M2 samples. This resulted in an error for all M2 velocities of $\pm 9.5 \text{ km s}^{-1}$. For 33 PN where velocity information did not exist, we adopted a value of the average velocity of *all* other PN in the $10^\circ \times 10^\circ$ which have velocities from D98 or M10, and adopt the standard deviation of the distribution as an estimate of the error.

Errors calculated for the system sensitivity were determined by taking the standard deviation of all individual measurements from each standard star. The errors due to the sampling of the filter profile were calculated from the 1.2 Å incremented transmission curve determined by NOAO (see fig. 1). There was also the possibility that the shape of the transmission curve had altered due to filter ageing. The possible influence of this effect is assessed in section 4.2.

The only other source of error we were not able to account for was the component dependent on which regions of sky were chosen. This was a function of how cleanly the sky had been subtracted, and the size of the sky regions selected.

After the off-band image had been scaled to and subtracted from the on-band image, the colour differences in the stars would often leave positive and negative residuals. Differences in seeing and focus between on- and off-band fields also resulted in imperfect alignment which accentuated any image residuals. This results in a broader range of sky values contributing to the sky background determination. Therefore, for PN in very crowded fields, there was an increased likelihood that slight deviations in non-perfect subtraction would amount to a larger error in the sky background. This source of error would dominate for PN with large angular diameters, where it was necessary to extract equivalent areas of sky, as it was likely that the sky areas chosen would include more artefacts.

Therefore, for PN in regions of high stellar number density, and particularly of large angular diameter, there would be larger errors associated with the average value of the background sky, and subsequently in the measured flux. This is potentially the dominant source of error, and is discussed further in section 4.2 below.

4.2 Comparison of duplicate observations of PN

During this project we obtained 62 duplicate observations of PN, whether on the same night (a), different nights within the same run (b), or different runs (c). To ensure appropriate error assignments determined from the previous section, differences between multiple $\log F$ measurements were calculated and are presented in Fig. 4.

Circled points from the lower panel of Fig. 4 are excluded from the final comparison as for these two points the seeing was significantly higher for one epoch, which led to large discrepancies between compared fluxes. Indeed, fluxes of the PN observed in fields of poorer seeing were found to be consistently fainter. This was the case for these two PN, where differences between their measurements were 0.060 and 0.046. Both data points were constituents of group (c). Careful comparison of the seeing conditions in all fields revealed that there were only two instances where the fields had significantly worse seeing (~ 2.5 arcsec as opposed

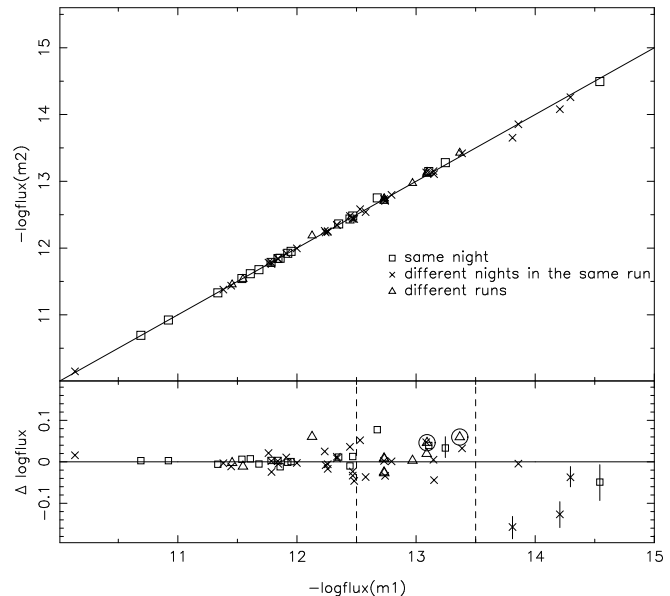


Figure 4. Comparison of observed [OIII] $\lambda 5007$ fluxes obtained for repeat measurements of PN. Shapes of the data points signify whether the measurements were from fields observed in the same night, for a different night during the same run, or different runs. Errors between measurements have been plotted for individual points when they exceed ± 0.025 , otherwise the error is indicated by size of the point. The dashed lines indicate the boundary between regions encompassing similar $\delta \log F$ measurements.

Table 2. Three regions in the $\Delta \log \text{flux}$ distribution have been identified. The range in $-\log F$, standard deviation and number of data points in the group are tabulated.

$-\log F$ range	σ	N
$-\log F \leq 12.5$	0.02	36
$12.5 < -\log F \leq 13.5$	0.03	19
$13.5 < -\log F \leq 15$	0.09	5

to ~ 0.7 arcsec seeing). Please note that PN with fluxes measured on either of these fields will be published with an error of ± 0.063 in the $\log F$. However, measured fluxes were discarded if the PN has a repeat flux measurement in another field with considerably better seeing conditions.

By comparing all duplicate measurements, there appears to be trends fitting three distinct regions in the flux error distribution. These are divided via the dashed lines in Fig. 4, with their sample sizes and standard deviation of all points in each region presented in Table 2. To ensure we have included all small systematic deviations in our error assignment, we designate these standard deviations as the error in our $\log F$ measurements, apart from those PN where their error from low S/N dominates. Here, their individual calculated errors are quoted.

The uncertainty in the sky subtraction is expected to increase as a function of the stellar number density in the field in which the PN is situated, and the angular diameter of the PN (since it was necessary to extract an equivalent

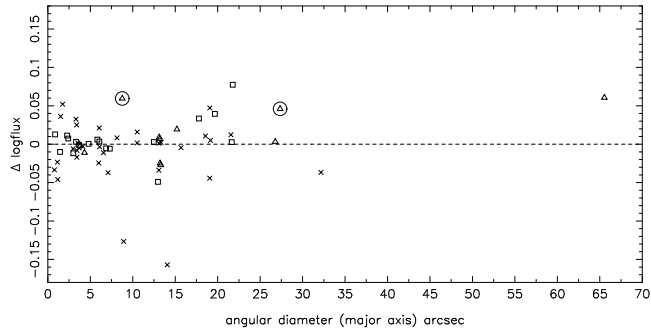


Figure 5. PN angular diameters are compared to the difference in flux between repeat measurements. The symbol shapes are the same as in Fig. 5. The difference between duplicate flux measurements is seen to be independent of angular diameter of the PN.

area of sky), as described towards the end of section 4.1. The difference in flux between two measurements is therefore proportional to the stellar number density of the environment and the angular diameter of the PN. Fig. 5, however, shows no angular diameter dependency exists with $\Delta \log F$. Extended PN are not observed to have significantly larger differences between duplicate flux measurements than smaller, more compact PN.

An error that we were unable to account for was the extent to which the transmission curve of the filter may have altered due to ageing since the initial measurement of the filter transmission curve. Ageing effects slow down quickly after the filter is made, with filters of this type becoming stable after a few years. The filters used here are >12 years old, so we do not expect a shift in the filter transmission curve to occur in our one year run-to-run separation between our measurements.

Instead, a significant shift of the transmission profile due to filter ageing would result in a more substantial deviation of our fluxes when compared to those from the literature, as a function of radial velocity. We refer the reader to section 4.3 for a full description of the literature sources that we have compared our data to. Fig. 6 plots the difference between fluxes published here and those collated from the literature, $\Delta \log F$, against the radial velocity of individual PN. The black data-points represent PN where comparison is drawn against an [OIII] $\lambda 5007$ flux from the literature, and are considered to be the most reliable. Red and blue data-points are those where an [OIII] $\lambda 5007$ flux has been calculated from either a $H\alpha$ or $H\beta$ flux combined with a relevant line ratio. Whilst considering the most reliable points, it is seen that there is no inclination for $\Delta \log F$ to bias towards a particular radial velocity. We therefore conclude that potential errors due to the ageing of the filter transmission profile are negligible.

4.3 Comparison with literature fluxes

To determine any systematic offset our data may be subject to, we compared our observed [OIII] $\lambda 5007$ fluxes to those PN with published fluxes from the literature. Of the PN we observed, 104 had previously published [OIII] $\lambda 5007$,

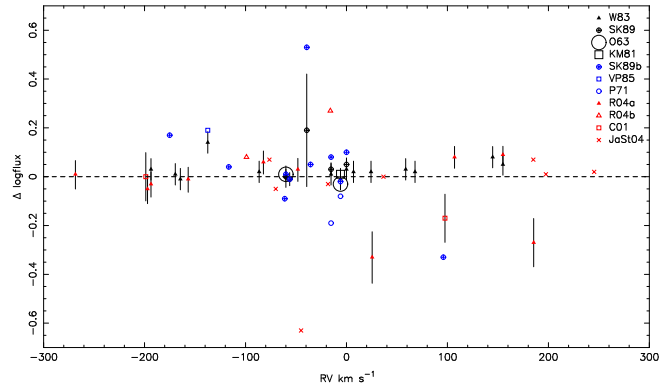


Figure 6. PN radial velocities are compared to the difference between the flux measurement published here and that collated from the literature. Black markers indicate where the literature flux was measured from [OIII] $\lambda 5007$ media, whilst red and blue represent those fluxes that have been transformed to an [OIII] $\lambda 5007$ flux from a $H\alpha$ or $H\beta$ flux, respectively. The shape of the data-points signify which literature source the comparison has been drawn from. Whilst considering comparisons against only the most reliable sources, no dependency on $\Delta \log \text{flux}$ with PN radial velocity is observed. This infers a negligible error contribution from any alteration in the filter transmission curve due to ageing, which would otherwise accentuate $\Delta \log F$ with PN velocity.

[OIII] $\lambda 4959$, $H\alpha$ or $H\beta$ fluxes with a [OIII] $\lambda 5007/H\alpha$ or [OIII] $\lambda 5007/H\beta$ line ratio where applicable. Significant contributions in this region have been made by Webster (1983), Kinman, Feast, & Lasker (1988), Shaw & Kaler (1989), Acker et al. (1991), Ruffe et al. (2004) and Jacoby & Van de Steene (2004) hereafter W83, KFL88, SK89, ASTR91, R04 and JaSt04 respectively, while fewer have been collated from O’Dell (1963), Kohoutek & Martin (1981), Cappellaro et al. (2001), Perek (1971) and Viadana & de Freitas Pacheco (1985) hereafter O63, KM81, C01, P71 and VP85 respectively. Absolute fluxes from the literature have been measured using either photoelectric narrow-band interference filter photometry (e.g. W83, SK89), CCD photometry (e.g. C01, R04) or from photographic plates (KFL88). Photographically derived fluxes are unfortunately subject to large errors, and are occasionally completely erroneous. Fluxes taken from the literature have only been included if their errors are quoted as being ≤ 0.3 dex. This excludes a substantial fraction of flux measurements of PN with angular diameters $\gtrsim 7$ arcsec from the ASTR91 sample. They publish global $H\beta$ fluxes as measured for PN with angular diameters smaller than the slit aperture, whereas fluxes for larger objects were calculated via multiplication by the geometric ratio of the size of the aperture and diameter of the PN. This led to an increased error for PN with angular diameters larger than the slit aperture.

It was necessary to place all of the older data onto the modern photometric scale so their fluxes reflect the most recent Vega calibration. This requires a correction of -0.02 for all sources apart from W83, which require an offset of -0.03 , while SK89 and ASTR91 need no such correction. Offsets are those derived from the recalibrated nebular fluxes as de-

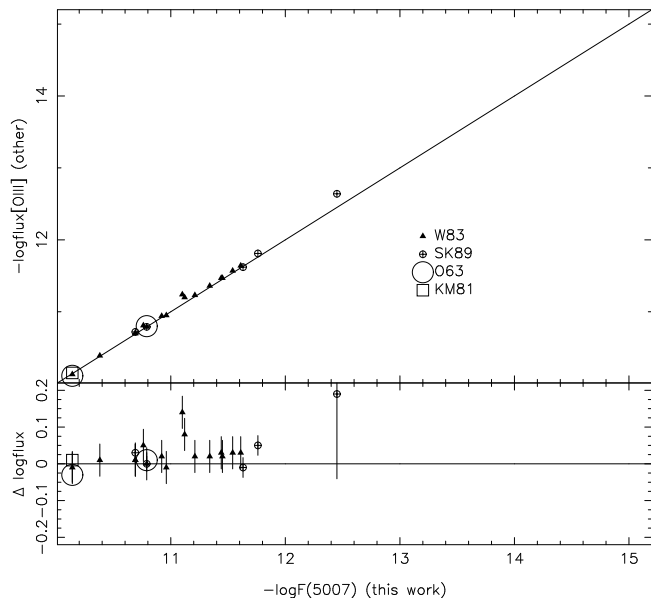


Figure 7. Our measured [OIII] $\lambda 5007$ fluxes compared against other directly measured [OIII] $\lambda 5007$ fluxes compiled from the literature. The triangles are data from W83, crossed circles are those from SK89, the two larger circles are data from O63 and the single square is from KM81.

scribed in Shaw & Kaler (1982), and are the same offsets implemented by Cahn, Kaler, & Stanghellini (1992).

We divide the literature sources into three groups, those which have either a direct [OIII] $\lambda 5007$ or [OIII] $\lambda 4959$ flux, which we shall consider to be the most reliable, those where an [OIII] $\lambda 5007$ flux has been transformed via combination of spectroscopy and $H\beta$ or $H\alpha$ photometry, and lastly those whose [OIII] $\lambda 5007$ fluxes were purely derived spectroscopically, e.g. via multiplication of an aperture correction, which we shall consider to be the least reliable.

O63, KM81 and W83 provide direct measurement of [OIII] $\lambda 5007$ integrated PN fluxes, while SK89 have published [OIII] $\lambda 4959$ fluxes, which are converted into an [OIII] $\lambda 5007$ flux via multiplication by the theoretical value for the [OIII] $\lambda 5007$ /[OIII] $\lambda 4959$ line ratio of 2.98 as given in Storey & Zeippen (2000). This sample is illustrated in Fig. 7. Note that there may be multiple data points for one object, as the brighter objects usually have published fluxes from more than one source. This aims to provide a comparison of integrity between literature sources in addition to the comparison to our own. It can be seen that the majority of fluxes agree with each other to ± 0.04 in the log. Considering that the errors from W83 are quoted as ± 0.04 , O63 are ± 0.01 , KM81 are ± 0.01 and those from SK89 are ± 0.02 and greater, our data are accurate to within the errors of these previously published sources. The SK89 data point at ~ -12.5 has a larger quoted error of ± 0.23 , so is still in agreement.

A secondary, slightly less reliable comparison was made with $H\alpha$ (JaSt04, R04, C01) and $H\beta$ (SK89, P71, VP85) fluxes measured from photometry. Their transformation to a [OIII] $\lambda 5007$ flux was calculated via multiplication of their [OIII] $\lambda 5007/H\alpha$ or [OIII] $\lambda 5007/H\beta$ ratios. Spectroscopic

line ratios were preferentially taken from data published by Cuisinier et al. (2000), or Górný et al. (2009) and ASTR91 in the absence of these. C01 published line ratios as well as fluxes, so their own line ratios were used here. Unpublished spectroscopy (van de Steene & Jacoby 2003) for the JaSt04 PN were used to boot-strap their $H\alpha$ fluxes to an [OIII] $\lambda 5007$ flux. The comparison of these transmogrified fluxes against our measurements are illustrated in Fig. 8. Note that the $\Delta \log F$ scale is significantly larger than that in Fig. 7.

The third, least reliable comparison was made where $H\beta$ fluxes had been derived spectroscopically (ASTR91 and KFL88). These fluxes are subject to significant additional error due to the aperture corrections made, and therefore can be considered less reliable than the previous comparisons. Due to this we include their comparison as fainter data points in Fig. 8. Note that the [OIII] $\lambda 5007$ fluxes included from ASTR91 are those with $H\beta$ fluxes provided by the authors, not the averaged value compiled from previous literature sources.

As noted by W83, the $H\beta$ fluxes of P71 depend strongly on the [OIII] $\lambda 5007/H\beta$ ratio as the [OIII] $\lambda\lambda 4959, 5007$ lines contribute 80 per cent to the $H\beta$ flux deduced from the P71 filter transmission curve. Therefore, we only include their published data for completeness, and do not give any weight to the comparison. We notice that, for fluxes measured by ASTR91 and KFL88, there tends to be an under-estimation of the brightness for PN with decreasing brightness compared to our new fluxes.

Note the [OIII] $\lambda 5007$ fluxes calculated from the recent, more reliable CCD data (R04, JaSt04 and C01) add valuable additional data points to test the integrity of the fluxes of fainter PN in the sample. Error bars have been included where they exist for both $H\alpha$ flux and spectroscopic line ratio. The R04 sample has been divided into two groups, one where an error has been calculated from the published flux and line ratio and the other where an error has not been calculated due to lack of error information. The JaSt04 data is in very close agreement with our data, bar one point with $\Delta \log F \sim -0.6$. Closer analysis of this individual PN, JaSt65, reveals that this large discrepancy is due to its location in the diffraction halo of a nearby bright star.

The comparison between our fluxes and those derived from $H\alpha$ flux data is accurate within the errors for PN with fluxes $\lesssim 13.6$ in $-\log F$. Although it appears errors published in this work for $-\log F \gtrsim 13.6$ have been under-estimated, there is still good agreement with published fluxes up to 15.0 in $-\log F$ once slightly larger error estimates have been applied. The errors could potentially be as large as 0.2 in this, but we adopt 0.09 given the confidence in our data comparison with the best sources at brighter flux limits.

Table 3 displays a comparison between our fluxes and those published from various literature sources. The horizontal division highlights the difference between those published [OIII] $\lambda 5007$ fluxes that have been measured directly and those that used a combination of $H\alpha$ or $H\beta$ flux and spectroscopic line ratios to calculate an [OIII] $\lambda 5007$ flux. The columns list the literature comparison source, the average difference in $\Delta \log F$ between measurements, the stan-

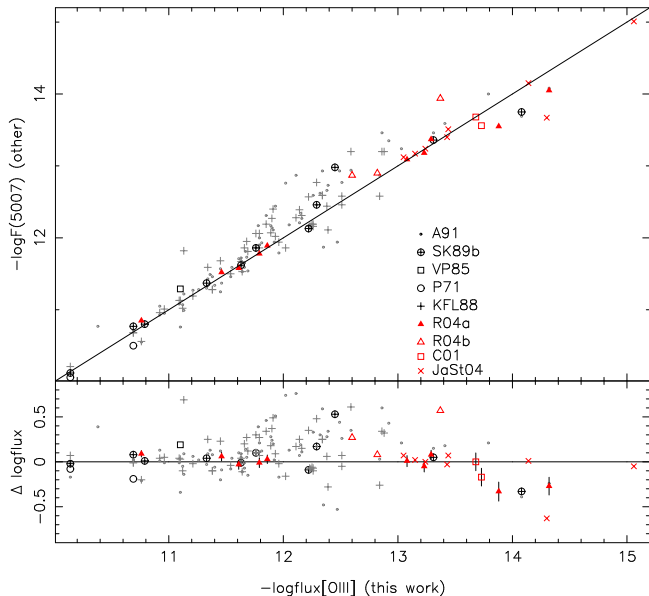


Figure 8. A comparison between our [OIII] $\lambda 5007$ fluxes to bootstrapped [OIII] $\lambda 5007$ fluxes from the literature. Red data-points signify those that have been transformed from a $H\alpha$ flux, whereas those in black are from a $H\beta$ flux. The R04 data has been grouped into those where errors exist for both $H\alpha$ flux and spectroscopic line ratio (filled triangles), and those where they don't (open triangles). The JaSt04 data point with $\Delta \log F$ of ~ -0.6 is not typical due to the location of the PN (see text).

standard deviation of errors and how many points are included in the analysis. There is a very clear difference between the two comparisons; the directly measured photoelectric fluxes and higher quality CCD bootstrapped fluxes can clearly be seen to agree far better with our dataset. There is a tendency for our fluxes to be slightly brighter than what has been previously published. This can be seen most noticeably in the comparison of the W83 data, where ours appear constantly offset by 0.03 dex.

4.4 Correcting for extinction and provision of dereddened fluxes

During our MASH PN identification programme follow-up, spectroscopy was obtained for 100 per cent of MASH bulge PNe. In principle these allow for Balmer decrement measurements and consequently can provide an estimate of the degree of extinction the [OIII] $\lambda 5007$ fluxes are subjected to. The AAOmega multi-object fibre spectroscopy system on the Anglo-Australian telescope (AAT) and the now decommissioned Double Beam Spectrograph on the MSSSO 2.3m were primarily used to obtain deep spectra for abundances and higher resolution spectra around $H\alpha$ for accurate radial velocities (Miszalski et al. 2011). As the multi-object facility on AAOmega allows for observation of ~ 400 objects over a 2-degree field-of-view (Lewis et al. 2002), fibres were also placed on previously known PN in the field enabling observation of most known PN in this region (see Table A2; see also Fig. 1 of Miszalski et al. 2009a).

Due to their fibre and dual-beam nature neither type of spectra are ideal for Balmer decrement estimates. Neverthe-

Table 3. Statistical comparison between fluxes measured here and literature sources. Tabulated are the average $\Delta \log F$ between measurements, the standard deviation of the differences and how many PN are in the sample. The horizontal division signifies the difference between sources who have published direct [OIII] $\lambda 5007$ fluxes (top), and those where [OIII] $\lambda 5007$ fluxes have been determined via calculation of the $H\alpha$ or $H\beta$ flux and spectroscopic line ratios.

Reference	$\overline{\Delta \log F}$	$\sigma_{\Delta \log F}$	N	type
O63	-0.01	0.02	2	PE
W83	0.03	0.04	16	PE
SK89	0.05	0.07	5	PE
KM81	0.01	-	1	PE
JaSt04	0.01	0.04	7	CCD
C01	-0.09	0.09	2	CCD
SK89	0.05	0.20	11	PE
P71	-0.14	0.20	2	PE
R04	0.04	0.21	14	CCD
KFL88	0.11	0.21	45	photographic
ASTR91	0.10	0.25	71	CCD
VP85	0.19	-	1	photographic

less, preliminary dereddened fluxes are presented in Table A2. The reader should treat these values with some caution, and we assign typical errors of ± 0.3 – 0.5 dex at this stage. A more detailed spectral analysis and improvements to these estimates are underway as better spectra become available. Full details of the spectroscopic analysis will be presented in Paper II, along with the fuller evaluation of the integrity of our dereddened fluxes.

5 ANGULAR DIAMETERS

As a by-product of this study, angular diameters were calculated for all observed PN that had detected [OIII] $\lambda 5007$ emission. Comparison between PN diameters within a co-located population serves as a proxy for their evolutionary state with those that are compact being younger than the more extended PN. Angular diameters can therefore be used to investigate whether bulge PN of certain evolutionary states occupy distinct regions in the PNLF.

Major and minor axes were measured using the 10 per cent level of maximum value method described in detail in Tyenda et al. (2003), hereafter T03.

In practice, the contouring algorithm in ds9 (Joye & Mandel 2003) was used to calculate 10 per cent increments of peak surface brightness, and the angular diameter was measured at the 10 per cent contour level. Due to the crowded stellar fields and non-perfect continuum subtraction, it was necessary to measure PN on an individual basis to ensure the peak brightness identified was that of the PN and not of an artefact. As the PN are often asymmetrical we have measured perpendicular axes, one being along the longest extension of emission. Fig. 9 displays examples of contours calculated for two PN in our sample: H2-36 and PPA1800-2904.

Note that this method is compromised for the compact PN in our sample, where the angular diameter measurement

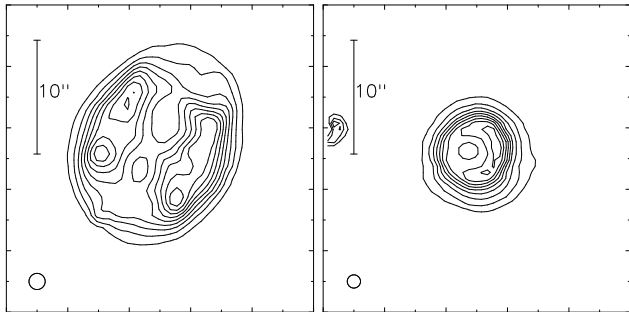


Figure 9. [OIII] $\lambda 5007$ images of PPA1800-2904 (left) and H2-36 (right) with contours at 10 per cent level increments of the maximum brightness of the PN. The images are 27×27 arcsec, with East up and North to the right. The circles in the bottom left hand corners represent the FWHM of the seeing disc.

is comparable to the angular resolution of the instrument, and those few observed in poor seeing. The observed angular resolution is a combination of the resolution of the camera and the natural seeing. These contributions needed to be deconvolved to obtain a true measurement of the PN. The full width at half-maximum (FWHM) of Gaussian fits to stars in each field were used to obtain the FWHM of the instrumental profile. This was then used to deconvolve the instrumental resolution component using equation (2) given in T03:

$$\Theta_{10 \text{ percent},d} = \sqrt{\Theta_{10 \text{ percent}}^2 - (1.823\Phi_b)^2} \quad (2)$$

where Φ_b is the FWHM of the resolution profile of the instrument, $\Theta_{10 \text{ percent}}$ is the angular diameter of the PN at the 10 per cent level and $\Theta_{10 \text{ percent},d}$ is the deconvolved PN diameter at the 10 per cent level.

5.1 Comparison of duplicate observations of PN

The errors in the measured angular diameters of PN were determined via comparison between duplicate major axes measurements for PN observed in more than one epoch during our survey. The difference in repeat measurements of a PN angular diameter (ΔD), is seen to be independent of measured diameter, so the standard deviation of the distribution (0.75 arcsec) is applied to all measurements as an estimate of the error.

5.2 Comparison with literature diameters

Prior to this work one of the most recent and homogenous compilations of bulge PN angular diameters was by T03 though their measurements are from $H\alpha$ images. However, provided the PNe can be considered optically thick, then the $H\alpha$ and [OIII] $\lambda 5007$ ionisation regions are comparable, so a direct comparison between their $H\alpha$ and our [OIII] $\lambda 5007$ angular diameters can be made as shown in Fig. 11. The majority of points are in good agreement apart from that of Hb 5. Hb 5 is a strongly bipolar nebula that is of similar morphology to the Homunculus around Eta Carinae. T03 note that such large discrepancies are

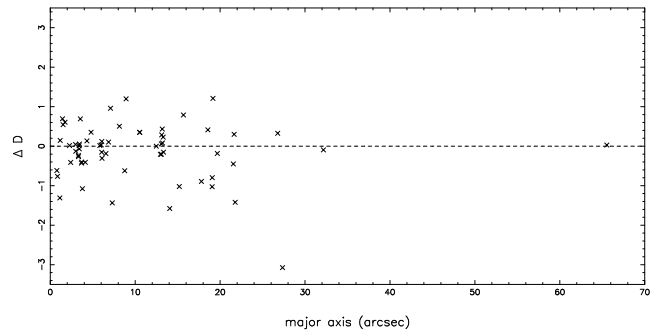


Figure 10. A comparison of angular diameters for 62 PN with duplicate measurements. The difference between duplicate measurements is seen to be independent of the major axis measured. The standard deviation of the distribution is the error assigned to all angular diameter measurements.

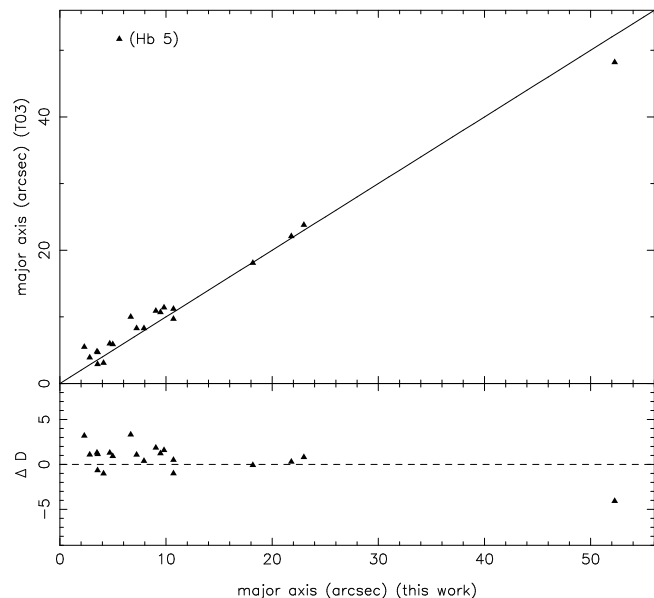


Figure 11. Our measured angular diameters compared against those from Tyenda et al. (2003). There is very good agreement except for data-point in the top left hand corner. This object is Hb 5, whose [OIII] $\lambda 5007$ 10 per cent contour level delineates the bright core as opposed to the $H\alpha$ diameter which encompasses the outer bipolar structure.

common in extended nebulae with bright bipolar cores. We therefore urge the reader to exercise caution when dealing with similar types of PN. In the case of Hb 5, their $H\alpha$ measurement encompasses a significant portion of outer bipolar structures, whereas our [OIII] $\lambda 5007$ diameter measurement only delineates the bright core. The smaller diameter in [OIII] $\lambda 5007$ is a consequence of ionisation stratification.

6 CONCLUSIONS

In this paper, we have increased the number of PN with directly measured [OIII] $\lambda 5007$ fluxes in the $10^\circ \times 10^\circ$

toward the Galactic bulge region by a factor of eight, with the addition of 387 previously unobserved PN. We have also re-observed 48 PN with directly measured [OIII] λ 5007 fluxes from the literature. Our new fluxes account for \sim 80% of known PN towards the Galactic bulge. We have provided additional fluxes for five PN in the peripheral regions, and for a special PN outside the bulge region (PHR1315-6555) that is the subject of another paper (Parker et al. 2010). This brings the total number of PN for which we have provided measured fluxes for to 441.

Photometric errors were derived via consideration of the S/N measurement, the velocities of the PN, the transmission profile of the filter curve and those due to the variation in the sensitivity factor calculated from the standard stars used. We found that these errors under-estimated the true error after comparison between duplicate measurements of a PN, so we increased the errors accordingly. We have compared our fluxes to all previously published [OIII] λ 5007, [OII] λ 4959, H α and H β fluxes, and found there to be no statistically significant systematic offset between the most trusted datasets and our new flux measurements to within the errors. Angular diameter measurements for all PN observed are also included, along with preliminary estimates of the dereddened fluxes based on the current best available spectra.

These data therefore provide accurate fluxes and angular diameters for the largest sample of PN in the $10^\circ \times 10^\circ$ region toward the Galactic bulge ever collated. Deriving from the same high quality, uniform, high resolution MOSAIC-II imaging, precise angular diameter measurements and greater insight into the fine morphological detail of each PN can be made. Combination of these factors will allow for the most detailed and accurate construction of the bulge PNLF to date. This will be the subject of Paper II.

ACKNOWLEDGMENTS

AVK acknowledges Macquarie University for a PhD scholarship. QAP and AVK wish to thank ANSTO for the travel grants which facilitated both observing trips to the CTIO BLANCO 4-m to collect this data. We thank NOAO for the award of telescope time. We acknowledge and thank Griet Van de Steene for allowing access to unpublished spectroscopic data for the JaSt PN. This paper has made use of the Simbad and VizieR database services, as well as the Aladin software tools. We thank Thomas Boch for writing the Aladin instrument FOV template for the MOSAIC-II camera. Thanks to Francois Ochsenbein for help with the PN G numbers. We thank an anonymous referee for some very valuable and useful comments.

REFERENCES

- Acker A., Raytchev B., Stenholm B., Tylenda R., 1991, *A&AS*, 90, 89
- Bohlin R. C., 1996, *AJ*, 111, 1743
- Bonnarel F., et al., 2000, *A&AS*, 143, 33
- Cahn J. H., Kaler J. B., Stanghellini L., 1992, *A&AS*, 94, 399
- Cappellaro E., Sabbadin F., Benetti S., Turatto M., 2001, *A&A*, 377, 1035
- Ciardullo R., 2003, *IAUS*, 209, 617
- Ciardullo R., 2010, *PASA*, 27, 149
- Ciardullo R., Feldmeier J. J., Jacoby G. H., Kuzio de Naray R., Laychak M. B., Durrell P. R., 2002, *ApJ*, 577, 31
- Ciardullo R., Sigurdsson S., Feldmeier J. J., Jacoby G. H., 2005, *ApJ*, 629, 499
- Clarkson W., et al., 2008, *ApJ*, 684, 1110
- Cuisinier F., Maciel W. J., Köppen J., Acker A., Stenholm B., 2000, *A&A*, 353, 543
- Cunha K., Smith V. V., 2006, *ApJ*, 651, 491
- Dopita M. A., Jacoby G. H., Vassiliadis E., 1992, *ApJ*, 389, 27
- Durand S., Acker A., Zijlstra A., 1998, *A&AS*, 132, 13
- Escudero A. V., Costa R. D. D., Maciel W. J., 2004, *A&A*, 414, 211
- Falcón-Barroso J., Peletier R. F., Balcells M., 2002, *MNRAS*, 335, 741
- Feldmeier J. J., Jacoby G. H., Phillips M. M., 2007, *ApJ*, 657, 76
- Feltzing S., Gilmore G., 2000, *A&A*, 355, 949
- Fouqué P., Solanes J. M., Sanchis T., Balkowski C., 2001, *A&A*, 375, 770
- Freyhammer L. M., Andersen M. I., Arentoft T., Sterken C., Nørregaard P., 2001, *ExA*, 12, 147
- Fulbright J. P., McWilliam A., Rich R. M., 2007, *ApJ*, 661, 1152
- Gerhard O., Arnaboldi M., Freeman K. C., Okamura S., Kashikawa N., Yasuda N., 2007, *A&A*, 468, 815
- Górny S. K., Chiappini C., Stasińska G., Cuisinier F., 2009, *A&A*, 500, 1089
- Górny S. K., Stasińska G., Escudero A. V., Costa R. D. D., 2004, *A&A*, 427, 231
- Hamuy M., Walker A. R., Suntzeff N. B., Gigoux P., Heathcote S. R., Phillips M. M., 1992, *PASP*, 104, 533
- Hayes D. S., Latham D. W., 1975, *ApJ*, 197, 593
- Irwin M., Lewis J., 2001, *NewAR*, 45, 105
- Jacoby G. H., Africano J. L., Quigley R. J., 1987, *PASP*, 99, 672
- Jacoby G. H., Ciardullo R., Ford H. C., 1988, *ASPC*, 4, 42
- Jacoby G. H., Ciardullo R., Ford H. C., 1990, *ApJ*, 356, 332
- Jacoby G. H., De Marco O., 2002, *AJ*, 123, 269
- Jacoby G. H., Van de Steene G., 2004, *A&A*, 419, 563
- Joye W. A., Mandel E., 2003, *ASPC*, 295, 489
- Kinman T. D., Feast M. W., Lasker B. M., 1988, *AJ*, 95, 804
- Kingsburgh R. L., Barlow M. J., 1994, *MNRAS*, 271, 257
- Kohoutek L., Martin W., 1981, *A&AS*, 44, 325
- Kovacevic. A. V. et. al., 2010, *MNRAS*, in prep.
- Kuijken K., Rich R. M., 2002, *AJ*, 124, 2054
- Kwok S., 2010, *PASA*, 27, 174
- Lecureur A., Hill V., Zoccali M., Barbuy B., Gómez A., Minniti D., Ortolani S., Renzini A., 2007, *A&A*, 465, 799
- Lewis I. J., et al., 2002, *MNRAS*, 333, 279
- Maciel W. J., Costa R. D. D., Uchida M. M. M., 2003, *A&A*, 397, 667
- Madore B. F., et al., 1999, *ApJ*, 515, 29

- Marigo P., Girardi L., Weiss A., Groenewegen M. A. T., Chiosi C., 2004, *A&A*, 423, 995
- Méndez R. H., Teodorescu A. M., Schönberner D., Jacob R., Steffen M., 2008, *ApJ*, 681, 325
- Merline W. J., Howell S. B., 1995, *ExA*, 6, 163
- Miszalski B., et al. 2011, *MNRAS*, in prep.
- Miszalski B., Acker A., Parker Q. A., Moffat A. F. J., 2009b, *A&A*, 505, 249
- Miszalski B., Acker A., Moffat A. F. J., Parker Q. A., Udalski A., 2009a, *A&A*, 496, 813
- Miszalski B., Parker Q. A., Acker A., Birkby J. L., Frew D. J., Kovacevic A., 2008, *MNRAS*, 384, 525
- Muller G. P., Reed R., Armandroff T., Boroson T. A., Jacoby G. H., 1998, *SPIE*, 3355, 577
- O'Dell C. R., 1963, *ApJ*, 138, 293
- Oke J. B., 1990, *AJ*, 99, 1621
- Ortolani S., Renzini A., Gilmozzi R., Marconi G., Barbuy B., Bica E., Rich R. M., 1995, *Natur*, 377, 701
- Parker Q. A., et al., 2010, *MNRAS*, submitted.
- Parker Q. A., et al., 2006, *MNRAS*, 373, 79
- Parker Q. A., et al., 2005, *MNRAS*, 362, 689
- Peletier R. F., Balcells M., Davies R. L., Andredakis Y., Vazdekis A., Burkert A., Prada F., 1999, *MNRAS*, 310, 703
- Perek L., 1971, *BAICz*, 22, 103
- Reid W. A., Parker Q. A., 2010, arXiv, arXiv:1002.3410
- Rich R. M., Origlia L., 2005, *ApJ*, 634, 1293
- Ruffle P. M. E., Zijlstra A. A., Walsh J. R., Gray M. D., Gesicki K., Minniti D., Comeron F., 2004, *MNRAS*, 353, 796
- Shaw R. A., Kaler J. B., 1982, *ApJ*, 261, 510
- Shaw R. A., Kaler J. B., 1989, *ApJS*, 69, 495
- Storey P. J., Zeppen C. J., 2000, *MNRAS*, 312, 813
- Torres-Peimbert S., Peimbert M., 1997, *IAUS*, 180, 175
- Tylenda R., Siódmiak N., Górny S. K., Corradi R. L. M., Schwarz H. E., 2003, *A&A*, 405, 627
- van de Steene G. C., Jacoby G. H., 2003, *IAUS*, 209, 49
- Viadana L., de Freitas Pacheco J. A., 1985, *RBrFi*, 15, 70
- Webster B. L., 1983, *PASP*, 95, 610
- Webster B. L., 1976, *MNRAS*, 174, 513
- Weidemann V., 2000, *A&A*, 363, 647
- Zoccali M., et al., 2006, *A&A*, 457, L1
- Zoccali M., et al., 2003, *A&A*, 399, 931

APPENDIX A: FIELD CENTRES AND FLUXES

Table A1. A list of the date field centres that were observed. All co-ordinates are J2000.

Field name (1)	RA (2)	Dec (3)	seeing (4)	exposure time (5)
9/6/2008				
F1753–2841	17 53 52.1	-28 41 15	2.04	3x400s
F1754–2915	17 54 04.8	-29 15 15	1.39	2x400s
F1751–2949	17 51 41.3	-29 49 15	1.26	3x400s
F1754–2949	17 54 17.9	-29 49 15	1.32	1x60s;3x400s
F1758–2733	17 58 34.3	-27 33 15	1.29	3x400s
F1804–2841	18 04 11.8	-28 41 15	1.26	1x60s;3x400s
F1759–2915	17 59 16.4	-29 15 15	1.16	3x400s
F1801–2841	18 01 36.9	-28 41 15	1.23	1x60s;3x400s
F1811–2807	18 11 38.5	-28 07 15	1.26	1x60s;3x400s
F1801–2807	18 01 22.0	-28 07 15	1.21	1x60s;3x400s
F1759–2841	17 59 01.9	-28 41 15	1.30	3x400s
F1802–3131	18 02 57.8	-31 31 15	1.42	1x60s;3x400s
F1803–2807	18 03 56.1	-28 07 15	1.52	3x400s
10/6/2008				
F1719–3048	17 19 44.8	-30 48 39	1.55	3x400s
F1751–2841	17 51 17.1	-28 41 15	1.33	3x400s
F1751–2915	17 51 29.0	-29 15 15	1.28	3x400s
F1753–2807	17 53 39.7	-28 07 15	1.42	3x400s
F1756–2841	17 56 27.0	-28 41 15	1.63	3x400s
F1756–2915	17 56 40.6	-29 15 15	1.27	3x400s
F1751–3023	17 51 53.8	-30 23 15	1.33	3x400s
F1806–2807	18 06 30.3	-28 07 15	1.23	3x400s
F1756–2807	17 56 13.8	-28 07 15	1.36	3x400s
F1758–2807	17 58 47.9	-28 07 15	1.29	1x60s;3x400s
F1756–2733	17 56 01.0	-27 33 15	1.25	3x400s
F1801–2733	18 01 07.6	-27 33 15	1.31	3x400s
F1806–2715	18 06 54.4	-27 15 54	1.45	3x400s
F1811–2722	18 11 18.8	-27 22 35	1.45	1x60s;3x400s
11/6/2008				
F1725–3055	17 25 26.8	-30 55 00	1.22	3x400s
F1804–2703	18 04 22.8	-27 03 33	1.14	1x60s;3x400s
F1806–2642	18 06 56.6	-26 42 03	1.15	1x30s;3x400s
F1801–2915	18 01 52.1	-29 15 15	1.24	3x400s
F1804–2915	18 04 27.9	-29 15 15	1.24	3x400s
F1807–2907	18 07 03.7	-29 07 21	1.12	1x30s;3x400s
F1807–2833	18 07 19.5	-28 33 20	1.09	1x30s;3x400s
F1752–3123	17 52 20.1	-31 23 21	1.10	3x400s
F1749–3015	17 49 16.3	-30 15 21	1.02	3x400s
F1749–3049	17 49 28.3	-30 49 21	1.23	1x30s;3x400s
F1804–2841	18 04 11.8	-28 41 15	1.21	1x60s;2x400s
F1806–2715	18 06 54.4	-27 15 54	1.22	2x400s
12/6/2008				
F1718–3006	17 18 37.7	-30 06 30	1.19	3x400s
F1800–2651	18 00 04.2	-26 51 17	1.22	3x400s
F1755–3025	17 55 04.8	-30 25 01	1.20	1x30s;3x400s
F1757–3115	17 57 34.9	-31 15 14	1.16	3x400s
F1754–3115	17 54 56.2	-31 15 02	1.14	3x400s
F1757–3149	17 57 12.9	-31 49 36	0.96	3x400s
F1758–3314	17 58 59.4	-33 14 21	0.96	1x30s;3x400s
F1751–3327	17 51 15.6	-33 27 01	0.99	3x400s
F1752–3401	17 52 58.4	-34 01 00	1.00	3x400s
F1750–3400	17 50 14.2	-34 00 54	1.03	3x400s
F1753–3435	17 53 52.8	-34 35 10	1.08	1x30s;3x400s
F1753–3518	17 53 24.9	-35 18 01	1.16	3x400s
13/6/2008				
F1722–2855	17 22 17.8	-28 55 39	1.63	1x30s;3x400s
F1740–3318	17 40 27.0	-33 18 58	1.48	3x400s
F1744–3302	17 44 06.9	-33 02 54	1.09	3x400s

Table A1 – continued

Field name (1)	RA (2)	Dec (3)	seeing (4)	exposure time (5)
13/6/2008				
F1743–3400	17 43 10.3	-34 00 44	1.28	1x30s;3x400s
F1752–3243	17 52 50.4	-32 43 53	1.19	1x30s;3x400s
F1743–2725	17 43 14.5	-27 25 21	1.05	3x400s
F1745–3428	17 45 36.6	-34 28 18	1.02	1x30s;3x400s
F1750–3203	17 50 43.4	-32 03 53	1.23	3x400s
F1800–2958	18 00 24.5	-29 58 21	1.05	3x400s
F1802–3049	18 02 52.8	-30 49 04	1.20	3x400s
F1803–2940	18 03 02.1	-29 40 31	1.10	1x30s;3x400s
F1805–3048	18 05 54.8	-30 48 24	1.19	1x30s;3x400s
F1800–3032	18 00 22.1	-30 32 36	1.15	3x400s
F1805–3014	18 05 38.4	-30 14 17	1.25	3x400s
F1811–2807	18 11 38.5	-28 07 15	1.40	1x60s;2x400s
F1811–2722	18 11 18.8	-27 22 35	1.48	1x60s;2x400s
14/6/2008				
F1722–3209	17 22 18.0	-30 29 41	1.81	3x400s
F1746–3200	17 46 58.8	-32 00 34	1.58	3x400s
F1802–3223	18 02 21.0	-32 23 31	1.29	3x400s
F1746–3325	17 46 47.6	-33 25 08	1.19	1x30s;3x400s
F1748–3450	17 48 04.4	-34 50 45	1.19	3x400s
F1751–3444	17 51 07.5	-34 44 17	1.18	1x30s;3x400s
F1757–3014	17 57 43.8	-30 14 17	1.60	1x30s;3x400s
F1800–2511	18 00 10.6	-25 11 37	1.42	1x30s;3x400s
F1803–3014	18 03 01.5	-30 14 37	1.27	1x30s;3x400s
F1757–2940	17 57 08.4	-29 40 26	1.32	1x30s;3x400s
F1759–3210	17 59 47.2	-32 10 04	0.94	1x30s;3x400s
F1752–3049	17 52 06.8	-30 49 21	1.14	1x30s;3x400s
F1746–3049	17 46 49.8	-30 49 21	1.15	3x400s
F1800–3106	18 00 14.7	-31 06 08	1.10	3x400s
F1811–2833	18 11 23.9	-28 33 37	1.26	1x30s;3x400s
27/6/2009				
F1748–2429	17 48 42.3	-24 29 29	2.68	3x400s
F1737–2802	17 37 51.7	-28 02 20	3.09	1x30s;3x400s
F1740–2759	17 40 29.5	-27 59 57	3.23	3x400s
F1730–3009	17 30 43.6	-30 09 06	2.00	3x400s
F1742–2542	17 42 40.9	-25 42 52	2.48	3x400s
F1736–2910	17 36 00.3	-29 10 32	2.69	3x400s
F1725–2929	17 25 18.5	-29 29 35	2.99	1x30s;3x400s
28/6/2009				
F1809–2905	18 09 58.7	-29 05 06	2.69	1x30s;3x400s
F1804–2637	18 04 16.7	-26 37 37	2.68	1x30s;3x400s
29/6/2009				
F1745–2619	17 45 38.3	-26 19 09	2.24	3x400s
F1735–2754	17 35 25.2	-27 54 27	2.15	3x400s
F1745–2543	17 45 03.6	-25 43 57	1.71	1x30s;3x400s
F1743–2651	17 43 03.6	-26 51 06	1.73	5x400s
F1739–2834	17 39 55.3	-28 34 54	1.74	3x400s
F1733–2942	17 33 28.9	-29 42 00	1.58	1x30s;3x400s
1/7/2009				
F1728–2755	17 28 49.5	-27 55 39	1.96	3x400s
F1731–2821	17 31 18.7	-28 21 02	1.89	1x30s;3x400s
F1730–2857	17 30 43.4	-28 57 54	2.04	1x30s;3x400s
F1728–2833	17 28 34.5	-28 33 30	1.81	1x30s;3x400s
F1740–2650	17 40 22.2	-26 50 05	2.02	2x400s
F1734–2641	17 34 09.7	-26 41 15	1.83	3x400s
F1729–2603	17 29 37.3	-26 03 39	2.08	3x400s
F1735–3019	17 35 30.6	-30 19 02	1.96	2x400s
F1737–2835	17 37 32.7	-28 35 38	1.85	2x400s

Table A1 – *continued*

Field name (1)	RA (2)	Dec (3)	seeing (4)	exposure time (5)
1/7/2009				
F1732–3015	17 32 58.5	–30 15 18	1.81	2x400s
F1743–2651	17 43 03.6	–26 51 06	1.76	1x100s
F1745–3401	17 45 23.3	–34 01 05	1.68	3x400s
F1810–2759	18 10 21.0	–27 59 08	1.62	3x400s
2/7/2009				
F1736–2328	17 36 17.8	–23 28 58	1.81	2x400s
F1740–2426	17 40 54.1	–24 26 53	1.73	1x30s;3x400s
F1738–2911	17 38 34.3	–29 11 29	1.71	3x400s
F1735–2945	17 35 57.8	–29 45 19	1.70	3x400s
F1740–2723	17 40 32.8	–27 23 56	1.53	3x400s
F1753–3435	17 53 52.8	–34 35 10	1.23	1x100s
F1748–3415	17 48 05.4	–34 15 19	1.20	1x30s;3x400s
F1756–3424	17 56 22.4	–34 25 58	1.26	1x30s;3x400s
F1757–3349	17 57 39.8	–33 49 22	1.31	1x30s;3x400s
F1743–2419	17 43 31.1	–24 19 33	1.37	1x30s;3x400s
F1748–2344	17 48 40.0	–23 44 33	1.39	2x400s
F1730–2722	17 30 58.4	–27 22 14	1.36	3x400s
F1737–2513	17 37 42.7	–25 13 56	1.53	3x400s
F1735–2711	17 35 27.1	–27 11 48	1.52	1x400s
F1810–2759	18 10 21.0	–27 59 08	1.78	1x30s
F1808–2938	18 08 07.6	–29 38 56	1.58	1x400s

Table A2. A table depicting our [OIII] $\lambda 5007$ global fluxes for 435 PNe in the $10^\circ \times 10^\circ$ region toward the Galactic Bulge. The PN G name and their common name are listed in the first two columns, the observed [OIII] $\lambda 5007$ flux measured directly from the CCD image is presented in column (3) (in $\text{erg cm}^{-2}\text{s}^{-1}$) with their estimated errors (4), with their preliminary dereddened fluxes in (5), and their major and minor axes are listed in columns (6) and (7). Diameters are subject to a $0.75''$ error, and dereddened fluxes are subject to an error of ± 0.3 – 0.5 dex.

PN G name (1)	Usual name (2)	$-\log(F[\text{OIII}])$			Diameter ($''$)		PN G name (1)	Usual name (2)	$-\log(F[\text{OIII}])$			Diameter ($''$)	
		Flux (3)	error (4)	F_{dered}^d (5)	maj (6)	min (7)			Flux (3)	error (4)	F_{dered}^d (5)	maj (6)	min (7)
000.0–01.3	PPA1751-2933	ND ^b	–	–	–	–	000.5+01.9	JaSt17	13.23	0.03	9.89	9.1	6.6
000.0–01.8	JaSt83	13.00	0.03	10.77	3.3	3.3	000.5+02.8	PHR1735-2659	12.76	0.03	–	26.5	25.6
000.0–01.8a	PHR1752-2953	13.26	0.03	–	17.8	16.8	000.5–03.1	MPA1759-3007	14.45	0.10	13.48	17.9	8.1
000.0–02.1	MPA1754-2957	13.05	0.03	11.09	21.5	19.0	000.6–01.0	JaSt77	13.43	0.03	7.89	10.3	9.6
000.0–02.5	K6-36	12.91	0.03	11.06	10.5	9.8	000.6–01.3	B13-15	15.39	0.22	12.47	3.9	1.2
000.0+01.3	JaSt27	ND ^b	–	12.85	–	–	000.6–01.4	PHR1753-2905	13.37	0.03	11.30	14.5	14.5
000.0+02.0	K6-4	14.97	0.21	10.96	6.9	4.1	000.6–01.6	MPA1753-2916	ND ^{ab}	–	–	–	–
000.0–02.9	MPA1757-3021	ND ^{ab}	–	–	–	–	000.6–04.5	PM1-206	13.04	0.03	11.50	20.3	17.3
000.1–01.0	JaSt69	13.90	0.09	10.65	11.1	9.4	000.6+03.1	PHR1734-2644	13.36	0.03	–	16.7	15.5
000.1–01.1	M3-43	12.88	0.03	9.06	3.5	2.7	000.6–03.2	MPA1759-3004	12.59	0.03	–	30.2	30.1
000.1–01.2	JaSt75	14.37	0.09	9.47	2.9	1.9	000.7–00.8	JaSt74	ND ^b	–	–	–	–
000.1–01.7	PHR1752-2941	12.52	0.03	10.31	16.7	12.2	000.7–01.5	JaSt2-11	13.80	0.09	11.47	9.7	8.8
000.1–01.9	JaSt93	12.41	0.02	10.37	14.2	11.7	000.7–02.7	M2-21	10.96	0.02	–	2.8	2.8
000.1+01.9	PHR1738-2748	13.90	0.09	10.77	13.6	9.8	000.7–03.7	M3-22	11.63	0.02	10.81	11.7	7.9
000.1+02.0	PHR1738-2746	13.27	0.03	–	18.9	17.5	000.7+03.2	He2-250	12.29	0.02	–	6.7	4.9
000.1+02.6	Al2-J	12.61	0.03	10.46	11.4	8.9	000.7+04.7	H2-11	12.99	0.03	–	3.6	3.4
000.2–01.9	M2-19	12.22	0.02	10.53	6.7	6.1	000.8–00.6	JaSt71	ND ^b	–	–	–	–
000.2–01.9a	JaSt2-14	ND ^b	–	–	–	–	000.8–01.5	B10	ND ^b	–	–	–	–
000.2–02.3	B13-10	11.64	0.02	10.13	7.2	6.9	000.8+01.3	JaSt38	14.36	0.09	–	10.9	9.6
000.2–03.4	PHR1759-3030	12.91	0.03	11.95	21.2	18.2	000.9–01.2	JaSt84	14.06	0.09	11.72	13.8	3.6
000.2–04.6	Sa3-117	12.51	0.03	11.35	8.2	6.8	000.9–01.4	JaSt2-13	14.12	0.10	–	26.5	25.9
000.2+01.4	PBOZ26	14.14	0.09	–	3.2	3.0	000.9–02.0	B13-13	12.02	0.02	10.27	4.2	3.9
000.2+01.7	JaSt19	13.09	0.03	10.06	7.2	6.4	000.9–03.3	PHR1801-2947	12.97	0.03	11.72	35.1	31.2
000.2–04.0	MPA1802-3045	ND ^b	–	–	–	–	000.9–04.2	PHR1804-3016	12.61	0.03	11.82	11.5	11.3
000.3–01.6	PHR1752-2930	12.93	0.03	10.13	8.6	7.9	000.9–04.8	M3-23	11.09	0.02	–	13.6	12.5
000.3–02.8	M3-47	12.60	0.03	11.24	8.1	7.2	000.9+01.1	JaSt44	14.24	0.09	–	8.5	5.0
000.3+01.5	JaSt23	ND ^b	–	–	–	–	000.9+01.8	PPA1740-2708	14.10	0.09	10.67	3.4	3.1
000.3+01.7	JaSt21	14.00	0.09	–	19.2	18.9	000.9+02.1	MPA1739-2702	13.60	0.09	–	19.0	11.9
000.3+03.2	PHR1733-2655	13.09	0.03	–	20.8	10.9	001.0–01.2	JaSt87	13.92	0.09	–	25.4	17.6
000.3+03.4	PHR1733-2647	13.58	0.09	–	16.8	15.0	001.0–01.5	MPA1754-2847	14.47 ^a	0.09	–	15.7	11.1
000.3+04.2	PPA1730-2621	13.79	0.09	–	7.6	7.3	001.0–01.9	PHR1755-2904	11.90	0.02	10.26	20.3	14.6
000.3+04.5	PHR1729-2614	13.66	0.09	–	14.8	10.5	001.0–02.6	Sa3-104	12.84	0.03	11.00	1.7	1.3
000.3–03.4	MPA1800-3023	13.24	0.03	12.13	7.9	5.8	001.0+01.3	JaSt41	13.15	0.03	10.88	4.7	4.6
000.3–04.2	MPA1803-3046	13.74	0.09	12.94	23.7	20.5	001.0+01.4	JaSt2-4	ND ^b	–	–	–	–
000.3–04.2a	MPA1803-3043	13.32	0.03	12.52	36.6	36.2	001.0+01.9	K1-4	11.51	0.02	–	52.3	47.4
000.4–01.3	JaSt2-8	ND ^b	–	–	–	–	001.0+02.2	PPA1739-2652	ND ^b	–	–	–	–
000.4–01.9	M2-20	11.54	0.02	10.15	3.6	3.2	001.0+02.2	MPA1739-2652	13.66 ^a	0.09	–	21.9	21.4
000.4–02.9	M3-19	11.90	0.02	10.59	7.2	6.6							
000.4+04.4	PPA1729-2611	12.85	0.03	–	6.4	5.5							
000.5–01.5	JaSt2-9	14.14	0.09	10.76	8.9	6.1							
000.5–01.6	Al2-Q	12.56	0.03	10.39	7.8	7.6							
000.5–01.7	JaSt96	12.98	0.03	11.46	32.9	31.2							
000.5–03.1	KFL1	12.14	0.02	10.64	8.0	7.9							

^aThis paper includes fluxes for several additional new MASH-II PN to be published in Miszalski et al. (2011).

^bND = No [OIII] $\lambda 5007$ flux was detected.

^cHS = Seeing was too high to allow for accurate diameter measurement.

^d Preliminary estimate of dereddened [OIII] $\lambda 5007$ flux with typical errors of ± 0.2 dex based on the current best available spectra.

Table A2 – *continued*

PN G name (1)	Usual name (2)	– log(F[OIII])			Diameter (″)	
		Flux (3)	error (4)	F ^{d_{dered}} (5)	maj (6)	min (7)
001.1–01.2	PPA1753-2836	12.83	0.03	10.05	10.3	8.5
001.1–01.6	Al2-S	12.59	0.03	10.39	6.4	5.7
001.1–02.6	MPA1758-2915	12.95 ^a	0.03	–	24.4	22.9
001.1+01.6	JaSt34	ND ^b	–	–	–	–
001.1+02.2	MPA1739-2648	14.53	0.09	10.90	4.5	3.8
001.2–01.2	JaSt92	14.22	0.09	–	9.5	4.7
001.2–01.2a	JaSt95	13.05	0.03	9.94	10.3	8.6
001.2–01.4	JaSt2-15	14.05	0.11	–	–	–
001.2–02.0	PHR1756-2857	13.90	0.09	–	22.7	17.0
001.2–02.6	PHR1759-2915	ND ^b	–	–	–	–
001.2–03.0	H1-47	14.18	0.09	12.55	1.1	0.9
001.2–03.8	PHR1803-2947	12.70	0.03	–	48.7	48.1
001.2–03.9	KFL5	11.76	0.02	10.73	1.3	1.1
001.2+01.3	JaSt45	13.98	0.09	–	31.3	30.6
001.2+02.1	He2-262	12.35	0.02	10.07	4.6	4.5
001.3–01.0	JaSt89	13.57	0.09	–	9.5	6.7
001.3–01.2	Bl1-M	14.08	0.09	10.88	3.5	3.5
001.4–04.4	BMP1806-2958	12.89	0.03	–	37.6	35.6
001.4–03.4	ShWi1	12.45	0.02	9.63	16.3	15.2
001.5–01.1	JaSt2-12	ND ^b	–	–	–	–
001.5–01.6	PHR1755-2825	14.52	0.09	–	13.0	1.2
001.5–01.8	JaSt2-19	14.20	0.09	11.14	5.3	2.7
001.5–02.4	PHR1758-2852	12.70	0.03	11.23	17.2	14.4
001.5–02.8	PPA1800-2904	12.45	0.02	11.20	9.8	9.8
001.5+01.5	JaSt46	13.24	0.03	10.73	4.5	4.4
001.6–01.0	JaSt90	ND ^b	–	–	–	–
001.6–01.1	JaSt97	14.54	0.09	–	7.4	5.6
001.6–01.3	BlQ	12.51	0.03	9.12	3.8	3.6
001.6–01.5	JaSt2-16	13.94	0.09	13.22	6.7	6.1
001.6–02.6	PHR1759-2853	12.75	0.03	11.12	22.6	21.3
001.6–03.7	MPA1804-2926	12.97 ^a	0.03	12.35	34.5	24.3
001.6+01.5	JaSt42	13.44	0.03	10.81	6.7	6.1
001.6+01.6	MPA1743-2636	ND ^b	–	–	–	–
001.7–01.6	H2-31	ND ^b	–	–	–	–
001.7–02.6	PPA1800-2846	12.00	0.02	10.91	15.1	12.6
001.8–03.8	ShWi7	12.25	0.02	11.46	16.0	2.0
001.7–04.4	H1-55	13.31	0.03	–	13.8	13.6
001.7–04.6	H1-56	11.33	0.02	–	4.2	4.2
001.8–01.5	JaSt2-18	ND ^b	–	–	–	–
001.8–02.0	PHR1757-2824	13.13	0.03	10.44	19.3	8.0
001.8–02.7	PHR1800-2842	13.12	0.03	11.98	11.3	10.1
001.8–03.2	MPA1802-2900	12.85	0.03	12.05	22.4	21.4
001.8–03.7	PHR1804-2913	12.91	0.03	12.15	8.3	7.3
001.9–02.5	PPA1759-2834	13.24	0.03	11.68	15.6	13.5
001.9–03.1	MPA1802-2850	ND ^{ab}	–	–	–	–
002.0–01.3	JaSt98	13.69	0.09	9.33	2.0	1.7

PN G name (1)	Usual name (2)	– log(F[OIII])			Diameter (″)	
		Flux (3)	error (4)	F ^{d_{dered}} (5)	maj (6)	min (7)
002.0–02.0	H1-45	11.96	0.02	–	1.5	1.1
002.0–02.1	MPA1758-2816	ND ^{ab}	–	–	–	–
002.0–02.4	MPA1800-2825	13.52	0.09	12.19	14.2	12.5
002.0–02.5	PPA1800-2826	12.71	0.03	11.50	21.8	18.8
002.0–03.1	PHR1802-2847	12.77	0.03	11.69	19.5	18.2
002.0–03.2	PHR1803-2848	12.56	0.03	12.70	32.2	28.4
002.0–03.4	PPA1803-2855	13.11	0.03	12.53	19.1	18.6
002.0+01.5	PHR1744-2624	14.45	0.11	–	11.1	8.7
002.1–01.1	MPA1755-2741	14.66	0.10	–	8.8	8.2
002.1–02.2	M3-20	11.21	0.02	–	4.0	3.2
002.1–02.4	PPA1800-2818	12.53	0.03	–	13.2	11.3
002.1–02.8	PHR1801-2831	12.51	0.03	11.16	18.5	16.4
002.1–03.8	MPA1805-2902	13.17 ^a	0.03	12.15	29.8	26.9
002.1–04.1	PHR1806-2909	12.87	0.03	12.35	28.1	27.7
002.1–04.2	H1-54	11.10	0.02	–	1.9	1.6
002.1+01.2	MPA1745-2626	ND ^b	–	–	–	–
002.1+03.3	–	13.66	0.09	–	5.8	5.2
002.2–01.2	PPA1755-2739	13.73	0.09	–	7.1	5.8
002.2–02.5	KFL2	12.38	0.02	11.14	8.2	5.9
002.2–04.3	PHR1808-2913	12.79	0.03	–	2.2	2.1
002.3–01.7	PPA1757-2750	ND ^b	–	–	–	–
002.3–01.9	PHR1758-2756	13.33	0.03	–	19.9	18.3
002.3–03.4	H2-37	11.78	0.02	10.69	6.0	3.5
002.3+01.7	PHR1744-2603	14.00	0.09	11.47	8.8	8.1
002.3+02.2	K5-11	13.01	0.03	10.79	10.2	9.1
002.3+02.4	PPA1741-2538	13.13	0.03	11.20	8.5	6.8
002.3+03.6	PPA1737-2501	13.12	0.03	–	6.4	6.2
002.4–02.6	PHR1801-2809	14.05	0.09	12.64	32.6	29.4
002.4–03.1	PPA1803-2826	12.00	0.02	10.78	4.1	3.2
002.4–03.2	Sa3-115	11.92	0.02	10.89	18.6	15.4
002.4–03.4	PHR1804-2833	12.56	0.03	–	1.7	0.4
002.4–03.7	M1-38	13.21	0.03	12.78	3.7	2.6
002.4+02.1	PHR1743-2541	13.83	0.09	11.67	14.9	11.2
002.4+03.5	PHR1738-2500	13.66	0.09	–	15.7	14.3
002.5–01.5	MPA1757-3532	14.53 ^a	0.10	–	14.7	12.5
002.5–01.7	Pe2-11	12.86	0.03	10.66	7.2	6.5
002.5–02.6	MPA1802-2803	13.57 ^a	0.09	12.64	42.8	41.9
002.5+01.9	PHR1744-2545	13.86	0.09	11.40	15.7	13.0
002.5+02.0	PHR1743-2538	13.56	0.09	10.66	5.1	4.4
002.6–01.7	PHR1758-2729	13.38	0.03	11.00	8.7	6.5
002.6–02.5	MPA1801-2755	13.49 ^a	0.03	11.66	12.1	9.4
002.6–02.8	PHR1803-2804	13.66	0.09	12.21	39.2	17.2
002.6–02.8a	MPA1802-2807	13.13 ^a	0.03	11.68	40.3	37.4
002.6–03.1	PHR1804-2816	12.50	0.03	11.33	14.3	14.0
002.6–03.4	M1-37	13.41	0.03	–	0.8	0.7
002.6+02.1	K5-13	12.45	0.02	10.40	11.7	9.9

Table A2 – continued

PN G name (1)	Usual name (2)	Flux (3)	–log(F[OIII])		Diameter (″)	
			error (4)	F _{dered} ^d (5)	maj (6)	min (7)
002.6+02.3	PHR1742-2525	13.42	0.03	11.02	11.5	11.4
002.7–02.4	PPA1801-2746	14.01	0.09	12.46	11.5	8.5
002.7–03.7	PHR1806-2824	12.80	0.03	11.77	13.1	12.6
002.7–04.6	MPA1810-2851	15.01 ^a	0.18	–	3.0	1.4
002.7–04.8	M1-42	10.92	0.02	–	12.5	11.6
002.8+01.7	H2-20	13.79	0.09	11.59	2.8	2.7
002.7+01.7	PPA1745-2542	13.90	0.09	10.91	3.6	3.5
002.8–02.2	Pe2-12	13.88	0.09	12.34	8.3	1.8
002.8–04.1	PHR1808-2835	12.15	0.02	10.73	18.9	16.3
002.8+01.7	K5-16	12.76	0.03	10.31	11.8	8.9
002.9–01.8	MPA1759-2719	13.73 ^a	0.09	–	20.6	20.6
002.9–03.0	PHR1804-2757	13.03	0.03	11.84	47.3	40.4
002.9–03.3	PHR1805-2804	ND ^b	–	–	–	–
002.9–03.6	MPA1806-2812	ND ^{ab}	–	–	–	–
002.9–04.0	H2-39	11.68	0.02	–	6.9	4.7
003.0–03.6	MPA1806-2807	12.89 ^a	0.03	–	19.6	17.3
003.1–01.6	PHR1759-2706	13.47	0.03	11.10	30.5	29.9
003.1–02.1	PHR1801-2718	13.21	0.03	11.41	38.1	35.1
003.1+02.9	Hb4	10.79	0.02	–	9.8	7.5
003.1+03.4	H2-17	14.36	0.09	–	2.3	1.9
003.2–04.4	KFL12	12.24	0.02	–	3.4	3.1
003.3–04.4	PPA1810-2813	12.73	0.03	–	13.2	13.0
003.3–04.6	Ap1-12	12.52	0.03	–	–	–
003.4–01.8	PHR1800-2653	13.07	0.03	10.54	9.3	9.5
003.4–04.8	H2-43	12.46	0.02	–	1.1	0.9
003.4+04.3	PHR1737-2341	13.59	0.09	–	17.2	14.0
003.5–02.3	PHR1803-2702	ND ^b	–	–	–	–
003.5–02.4	IC4673	10.69	0.02	9.71	21.7	16.5
003.5–02.9	MPA1805-2721	13.10	0.03	12.25	31.1	22.2
003.5–04.6	NGC6565	10.14	0.02	–	10.5	9.6
003.5+02.6	PHR1743-2431	12.56	0.03	–	33.9	33.6
003.5+04.3	PPA1737-2341	ND ^b	–	–	–	–
003.5+04.5	PHR1736-2330	13.50	0.09	–	10.8	5.0
003.6–02.3	M2-26	11.91	0.02	10.56	9.5	9.4
003.6–02.8	MPA1805-2712	13.21	0.03	11.76	42.9	41.1
003.6–03.0	PHR1805-2723	12.34	0.02	11.26	21.6	19.9
003.6+02.7	PHR1743-2424	13.99	0.09	–	22.8	21.8
003.6+03.1	M2-14	11.85	0.02	–	3.0	2.6
003.6+04.9	K5-6	12.41	0.02	–	22.6	9.7
003.7–04.6	M2-30	10.76	0.02	–	5.1	5.0
003.8–02.4	PHR1804-2653	13.40	0.03	–	8.8	6.7
003.8–03.2	PHR1807-2715	14.06	0.09	–	12.4	10.0
003.8–04.3	H1-59	11.44	0.02	–	6.6	6.0
003.8–04.5	H2-41	11.79	0.02	–	10.5	9.6
003.9+02.6	K5-14	12.16	0.02	–	1.8	1.7
003.9–02.3	M1-35	11.33	0.02	–	7.3	6.8

PN G name (1)	Usual name (2)	Flux (3)	–log(F[OIII])		Diameter (″)	
			error (4)	F _{dered} ^d (5)	maj (6)	min (7)
003.9–03.1	KFL7	12.34	0.02	–	8.1	5.0
003.9+01.6		13.60	0.09	–	9.7	9.5
004.0–02.5	PHR1804-2642	13.41	0.03	11.45	15.0	12.6
004.0–02.6	PHR1804-2645	12.40	0.02	10.40	24.5	13.2
004.0–02.7	PPA1805-2649	13.11	0.03	11.46	27.4	22.1
004.0–03.0	M2-29	11.45	0.02	–	4.8	3.6
004.1–03.3	PPA1808-2700	12.38	0.02	–	13.1	8.5
004.1–03.8	KFL11	12.26	0.02	–	3.0	2.3
004.2–04.3	H1-60	11.38	0.02	–	6.1	5.6
004.1+01.7	PPA1748-2427	13.43	0.03	–	25.7	16.9
004.2–02.5	PHR1805-2631	12.48	0.02	10.41	12.5	10.3
004.2–03.2	KFL10	11.93	0.02	–	7.1	5.6
004.2+01.5	K6-29	13.18	0.03	–	10.8	7.7
004.2+02.0	K5-17	12.10	0.02	–	4.6	3.1
004.2+02.0a	MPA1747-2414	13.72	0.09	–	25.2	23.1
004.3–02.6	H1-53	12.36	0.02	10.46	2.3	1.7
004.3+01.8	H2-24	12.50	0.03	–	8.4	4.3
004.3+01.8a	PHR1748-2417	12.81	0.03	–	16.1	14.8
004.4–03.1	PHR1807-2637	13.15	0.03	–	25.4	25.3
004.5–03.0	MPA1807-2631	13.17 ^a	0.03	–	41.4	40.4
004.5+02.0	MPA1748-2402	13.27	0.03	–	12.9	9.4
004.6+01.8	BMP1749-2356	13.63	0.09	–	26.1	17.9
004.8–00.5	PHR1759-2501	13.04	0.03	–	42.3	26.4
004.8–01.1	PHR1801-2522	14.16	0.09	–	7.3	7.0
004.8+02.0	H2-25	13.41	0.03	–	3.1	3.0
355.0–03.3	PPA1746-3454	14.25	0.09	11.75	8.3	2.9
355.0–03.7	K5-18	12.28	0.02	11.04	11.1	10.0
355.1–02.9	H1-31	11.40	0.02	9.74	1.8	1.7
355.1+03.7	PHR1718-3055	13.09	0.03	11.58	20.8	19.9
355.2–02.0	PPA1741-3405	13.35	0.03	–	6.5	6.5
355.2–02.5	H1-29	11.61	0.02	10.25	2.4	2.2
355.2–05.0	PHR1754-3533	12.99	0.03	–	26.9	26.1
355.2+03.7	Th3-5	12.62	0.03	11.09	13.3	10.5
355.3–03.2	PPA1747-3435	13.34	0.03	11.98	19.5	15.4
355.3–04.1	PHR1750-3500	12.65	0.03	–	20.4	16.7
355.3+03.7	MPA1719-3043	12.67	0.03	–	72.6	72.2
355.4–01.4	K6-9	13.44	0.03	–	8.4	7.5
355.4–02.4	M3-14	11.45	0.02	10.05	3.8	3.6
355.4–02.6	PHR1745-3413	13.10	0.03	11.70	15.2	11.9
355.4–03.1	PPA1746-3428	12.97	0.03	–	26.8	24.2
355.4–04.0	Pe1-10	10.92	0.02	Pe1-10	18.2	14.0
355.4–04.3	K5-34	11.91	0.02	–	6.8	5.8
355.4+03.6	PHR1719-3044	13.34	0.03	11.65	20.0	15.6
355.5–01.1	MPA1739-3320	14.81	0.24	–	7.2	6.0
355.5–03.7	PHR1749-3438	12.31	0.02	11.00	19.6	13.2
355.5–04.8	PHR1754-3515	12.54	0.03	–	19.5	18.7

Table A2 – *continued*

PN G name (1)	Usual name (2)	$-\log(F[\text{OIII}])$			Diameter (")	
		Flux (3)	error (4)	$F_{d_{\text{ered}}}^d$ (5)	maj (6)	min (7)
355.5+03.6	PHR1720-3041	13.78	0.09	–	24.6	22.3
355.6–01.4	PHR1740-3324	13.52	0.09	–	11.8	9.6
355.6–02.3	PHR1744-3355	12.16	0.02	11.04	65.5	63.7
355.6+03.6	PHR1720-3038	13.07	0.03	11.11	15.2	14.9
355.6+04.1	PHR1718-3019	12.60	0.03	–	46.7	40.5
355.7–03.0	H1-33	11.63	0.02	10.40	4.0	3.2
355.7–03.4	H2-23	11.66	0.02	10.41	3.4	2.7
355.8+03.5	PHR1721-3027	13.06	0.03	10.78	13.5	8.8
355.8+04.5	PHR1717-2954	13.69	0.09	–	12.2	11.2
355.9–04.2	M1-30	11.54	0.02	–	4.3	3.6
355.9+02.7	Th3-10	13.08	0.03	9.96	3.0	2.6
355.9+03.1	PPA1723-3038	13.76	0.09	10.42	5.6	5.1
355.9+04.1	PHR1719-3003	13.28	0.03	–	23.5	23.0
356.0–01.4	PPA1741-3302	14.01	0.09	–	6.9	6.8
356.0–01.8	PPA1743-3315	13.77	0.09	–	4.9	4.4
356.0–04.2	PHR1753-3428	12.46	0.02	11.09	15.3	14.6
356.0+02.8	PPA1724-3043	13.97	0.09	10.71	10.6	9.3
356.1–02.1	PHR1744-3319	13.68	0.09	–	8.9	8.4
356.1–02.7	PPA1747-3341	13.97	0.09	11.17	7.3	7.0
356.1–03.3	H2-26	12.50	0.03	11.14	5.5	5.0
356.1+02.7	Th3-13	12.82	0.03	10.00	1.9	1.4
356.2–03.2	PHR1749-3347	13.58	0.09	12.16	12.8	12.5
356.2–03.6	PPA1751-3401	12.58	0.03	11.20	11.4	11.2
356.2–04.4	Cn2-1	10.38	0.02	–	2.6	2.6
356.2+02.5	PPA1726-3045	14.17	0.09	9.97	4.1	2.7
356.3–02.6	MPA1747-3326	12.74	0.03	11.29	8.1	7.3
356.4–02.5	K6-12	13.39	0.03	11.43	13.7	11.2
356.5–01.8	PPA1744-3252	13.82	0.09	–	4.6	4.4
356.5–02.3	M1-27	ND ^b	–	–	–	–
356.5–03.4	MPA1751-3339	13.11	0.03	11.23	8.1	8.0
356.5–03.6	H2-27	12.64	0.03	10.53	5.2	4.2
356.5–03.9	H1-39	12.92	0.03	–	2.3	2.0
356.5–04.1	PPA1754-3358	12.72	0.03	11.43	14.1	13.3
356.6–01.9	PHR1745-3246	12.61	0.03	–	51.6	34.4
356.6–04.7	PHR1756-3414	12.29	0.02	11.47	20.1	18.7
356.7–04.7	MPA1757-3410	12.79	0.03	11.85	12.0	11.3
356.7–04.8	H1-41	10.89	0.02	10.40	12.0	8.8
356.8–03.0	K5-20	12.36	0.02	10.70	5.3	5.2
356.8–03.6	PHR1752-3330	13.42	0.03	12.57	1.1	0.9
356.8+03.3	Th3-12	14.32	0.09	–	2.0	1.3
356.9+02.2	MPA1729-3016	13.50	0.09	11.69	7.0	6.9
356.9+04.4	M3-38	11.78	0.02	–	1.6	1.2
357.0–04.4	PHR1756-3342	13.16	0.03	11.57	21.6	20.9
357.1–04.7	H1-43	ND ^b	–	–	–	–
357.1+01.9	Th3-24	13.23	0.03	11.74	8.6	7.3
357.1+03.6	M3-7	11.61	0.02	–	6.5	6.0

PN G name (1)	Usual name (2)	$-\log(F[\text{OIII}])$			Diameter (")	
		Flux (3)	error (4)	$F_{d_{\text{ered}}}^d$ (5)	maj (6)	min (7)
357.1+04.4	PBOZ1	12.51	0.03	–	10.9	9.1
357.2–04.5	H1-42	10.54	0.02	–	4.3	3.7
357.2+01.4	A12-H	12.90	0.03	10.22	8.5	7.0
357.2+02.0	H2-13	12.05	0.02	9.86	5.6	5.4
357.3–02.0	PPA1747-3215	ND ^b	–	–	–	–
357.3+01.3	PHR1733-3029	13.86	0.09	–	17.4	17.1
357.3+02.3	K6-25	13.24	0.03	10.51	5.0	5.0
357.3+03.3	M3-41	14.06	0.09	–	HS ^c	HS ^c
357.3+04.0	H2-7	11.95	0.02	–	4.8	4.3
357.3+04.1	PHR1723-2856	13.38	0.03	–	20.7	18.9
357.4–03.1	PHR1752-3244	12.85	0.03	–	10.8	10.6
357.4–03.2	M2-16	11.36	0.02	10.35	3.1	2.9
357.4–03.5	M2-18	11.67	0.02	–	2.2	2.1
357.4–04.6	M2-22	11.54	0.02	10.42	5.8	5.2
357.4+03.4	PPA1725-2915	12.80	0.03	–	11.2	10.7
357.5–02.4	PPA1749-3216	13.68	0.09	–	7.8	6.5
357.5+01.3	PPA1734-3015	ND ^b	–	–	–	–
357.5+02.0	PPA1731-2955	13.55	0.09	–	19.0	12.4
357.6–03.0	PHR1752-3233	12.64	0.03	–	10.9	7.5
357.6–03.0a	PHR1752-3230	12.98	0.03	–	9.7	9.1
357.6–03.3	H2-29	13.29	0.03	11.50	9.0	8.0
357.6+01.0	TBJ4	12.98	0.03	10.64	31.5	26.8
357.6+01.7	H1-23	11.84	0.02	9.70	3.5	2.6
357.7–01.7		ND ^b	–	–	–	–
357.7–04.8	BMP1759-3321	ND ^b	–	–	–	–
357.7+01.4	PPA1734-3004	13.81	0.09	–	3.6	3.1
357.8–03.3	PHR1753-3228	11.75	0.02	10.32	65.1	40.1
357.8–04.4	PHR1758-3304	11.98	0.02	10.69	16.6	14.3
357.8+01.6	PPA1734-2954	14.01	0.09	–	12.7	8.6
357.9+01.7	PPA1733-2945	13.57	0.09	11.10	5.7	5.0
358.0–02.4	PPA1750-3152	13.66	0.09	–	4.9	3.7
358.0–02.7	A12-O	12.29	0.02	–	9.1	7.6
358.0–04.6	Sa3-107	12.42	0.02	10.82	6.3	5.9
358.0+01.5	JaSt1	14.28	0.09	11.87	7.1	5.1
358.0+01.6	PHR1734-2944	14.04	0.09	10.76	8.9	6.8
358.0+02.6	Th3-23	12.61	0.03	9.97	6.9	5.9
358.1+02.3	PPA1731-2915	14.80	0.20	–	3.8	1.5
358.2–01.1		12.53	0.03	–	17.5	15.7
358.2+03.5	H2-10	11.92	0.02	9.89	3.7	3.0
358.2+03.6	M3-10	11.13	0.02	–	4.2	4.0
358.3–02.5	M4-7	12.29	0.02	9.65	6.9	6.6
358.3+01.2	B1B	13.25	0.03	–	2.4	2.0
358.3+03.0	H1-17	11.63	0.02	9.53	2.8	2.8
358.4–02.3	MPA1751-3128	14.19	0.09	–	15.1	12.2
358.4+01.6	JaSt3	13.61	0.09	9.90	7.8	7.8
358.4+01.7	JaSt2	14.34	0.09	10.78	4.4	4.3

Table A2 – continued

PN G name (1)	Usual name (2)	–log(F[OIII])			Diameter (″)	
		Flux (3)	error (4)	F _{dered} ^d (5)	maj (6)	min (7)
358.4+02.7	PHR1731-2850	13.16	0.03	–	22.1	16.1
358.4+03.3	Th3-19	12.27	0.02	9.96	2.3	2.3
358.5–01.7	JaSt61	13.90	0.09	10.69	2.0	2.0
358.5–04.2	H1-46	11.26	0.02	–	1.5	1.2
358.5+02.6	K6-1	11.50	0.02	–	47.0	34.2
358.5+02.9	Al2-F	12.71	0.03	10.91	4.2	3.5
358.5+03.7	Al2-B	13.02	0.03	11.28	6.8	4.6
358.6–02.4	K6-16	13.66	0.09	11.07	8.9	8.2
358.6–03.6	PHR1756-3157	11.96	0.02	–	53.1	46.5
358.6+01.7	JaSt4	13.96	0.09	10.78	10.6	9.5
358.6+01.8	M4-6	12.43	0.02	9.80	4.1	4.0
358.7–02.5	PHR1752-3116	13.04	0.03	10.90	9.3	6.9
358.7–02.7	Al2-R	12.93	0.03	11.00	6.4	3.9
358.7–03.0	K6-34	13.53	0.09	11.80	10.4	9.8
358.8+01.7	JaSt5	13.44	0.03	10.64	9.1	5.9
358.8+03.0	Th3-26	12.15	0.02	10.53	9.1	8.3
358.8+03.4	MPA1729-2804	13.96	0.09	–	14.8	14.6
358.8+03.8	PHR1727-2747	13.56	0.09	11.42	16.2	14.4
358.9–01.5	JaSt65	14.30	0.09	10.36	5.7	5.6
358.9–02.1	PHR1751-3059	13.64	0.09	12.02	13.8	13.5
358.9–03.6	PPA1757-3144	12.85	0.03	–	13.8	6.3
358.9–03.7	H1-44	13.03	0.03	–	3.5	3.3
358.9+03.2	H1-20	11.81	0.02	9.74	4.4	3.8
358.9+03.4	H1-19	12.32	0.02	10.52	2.6	2.0
359.0–01.6	GLMP647	ND ^b	–	–	–	–
359.0–04.1	M3-48	12.39	0.02	–	4.7	4.2
359.0–04.8	M2-25	11.45	0.02	–	17.7	13.4
359.0–04.9	PHR1803-3218	12.69	0.03	–	35.1	30.2
359.0+01.1	JaSt9	14.71	0.22	13.62	6.4	2.4
359.0+02.8	Al2-G	13.15	0.03	10.82	3.5	1.0
359.0+03.0	MPA1731-2805	14.18	0.10	–	20.7	12.4
359.0+03.7	PHR1728-2743	13.40	0.03	10.75	18.4	17.6
359.1–01.7	M1-29	11.13	0.02	9.50	9.1	6.7
359.1–02.3	M3-16	11.66	0.02	10.09	10.0	7.7
359.1+02.9	MPA1732-2806	14.44	0.10	–	16.5	6.0
359.2–03.1	PHR1756-3112	13.00	0.03	11.45	16.6	13.4
359.2+01.2		13.66	0.09	9.13	23.0	4.7
359.2+01.3	JaSt8	14.10	0.09	–	8.0	6.7
359.3–00.9	Hb5	10.33	0.02	–	5.6	5.5
359.3–02.3	PHR1753-3038	13.73	0.09	–	14.1	11.3
359.3–02.8	MPA1755-3058	13.61	0.09	–	37.0	33.8
359.3–03.1	M3-17	12.83	0.03	11.38	3.0	2.9
359.3+01.3	JaSt12	14.53	0.13	–	3.9	2.4
359.3+01.4		13.40	0.03	9.69	3.3	2.6
359.3+01.4a	PHR1738-2847	14.45	0.09	–	6.9	6.3
359.3+03.6	Al2-E	12.41	0.02	9.96	8.8	8.0

PN G name (1)	Usual name (2)	–log(F[OIII])			Diameter (″)	
		Flux (3)	error (4)	F _{dered} ^d (5)	maj (6)	min (7)
359.4–03.3	PHR1757-3106	12.84	0.03	12.18	12.8	10.4
359.4–03.4	H2-33	12.11	0.02	10.60	7.9	7.3
359.4+02.3	Th3-32	ND ^b	–	–	–	–
359.4+02.3a	PPA1735-2809	13.93	0.09	10.33	4.5	2.9
359.4–03.7	MPA1759-3116	13.51	0.09	12.59	22.9	22.6
359.5–01.2	JaSt66	14.14	0.09	9.39	3.4	2.7
359.5–01.3	JaSt68	15.06	0.19	–	2.0	1.7
359.5–01.8	PHR1751-3012	14.64	0.11	12.64	38.0	32.1
359.5+02.6	Al2-K	12.44	0.02	9.94	5.6	4.8
359.5+03.5	MPA1730-2726	13.71	0.09	–	20.0	18.5
359.6–04.8	H2-36	11.85	0.02	–	17.7	14.5
359.6+01.0		14.69	0.09	10.01	3.0	2.4
359.6+02.2		13.40	0.03	10.06	4.7	4.5
359.7–01.4	JaSt73	15.06	0.19	12.19	1.2	0.7
359.7–01.7	K6-15	13.38	0.03	10.70	5.0	4.4
359.7–01.8	M3-45	11.89	0.02	9.69	7.1	6.5
359.7–02.2	PPA1753-3021	13.68	0.09	11.80	18.5	18.3
359.7–02.6	H1-40	11.69	0.02	–	1.4	1.4
359.7–04.4	KFL3	12.16	0.02	10.91	15.2	14.3
359.7–04.4a	PPA1802-3124	12.49	0.02	11.70	17.6	15.5
359.7+02.0	PPA1736-2804	13.55	0.09	9.60	4.3	3.6
359.8+01.0	JaSt2-3	ND ^b	–	–	–	–
359.8+02.4		14.49	0.09	11.56	HS ^c	HS ^c
359.8+03.5	PHR1731-2709	13.84	0.09	10.93	15.5	12.4
359.8+03.7		12.54	0.03	9.78	3.0	2.6
359.9–01.8	MPA1752-2953	13.86	0.09	12.02	24.6	20.5
359.9–02.6	PHR1756-3019	12.90	0.03	11.25	14.2	12.6
359.9–04.5	M2-27	11.12	0.02	–	3.3	3.0
359.9+01.7	JaSt2-2	14.20	0.09	11.15	12.3	9.7
359.9+01.8	PPA1738-2800	14.16	0.09	–	7.4	4.3

Table A3 – continued [OIII] λ 5007 fluxes for 5 PNe just outside our region toward the Galactic Bulge. All fluxes presented are uncorrected for interstellar absorption.

PN G name (1)	Usual name (2)	–log(F[OIII])			Diameter (″)	
		Flux (3)	error (4)	F _{dered} ^d (5)	maj (6)	min (7)
002.4–05.0	PHR1811-2922	11.88	0.02	–	27.6	27.1
003.0–05.0	PHR1812-2848	12.14	0.02	–	15.3	14.1
005.1+02.0	K5-19	12.41	0.02	–	6.7	3.6
305.3–03.1	PHR1315-6555	12.35	0.02	–	11.4	11.4
354.9–02.8	MPA1744-3444	13.21	0.03	11.58	9.5	8.5
358.7–05.1	SB53	11.98	0.02	–	14.4	11.6